

This paper is a non-peer reviewed preprint submitted to EarthArXiv.

1
2 Adrian P. Broz^{1,2§*}, Devin Pritchard-Peterson³, Diogo Spinola⁴, Sarah Schneider², Lucas C.R.
3 Silva^{5,6}, and Greg Retallack²

4
5 ¹ Department of Earth, Atmospheric and Planetary Sciences, Purdue University, Lafayette, IN

6 ²Department of Earth Sciences, University of Oregon, Eugene, OR

7 ³Dudek Environmental Consulting, Encinitas, CA

8 ⁴Department of Chemistry and Biochemistry, University of Alaska, Fairbanks, AK

9 ⁵Environmental Studies Program, University of Oregon, Eugene, OR

10 ⁶Department of Biological Sciences, University of Oregon, Eugene, OR

11

12 ***Correspondence:** abroz@uoregon.edu

13

14 *This paper is a non-peer reviewed preprint submitted to EarthArXiv.*

15

16

17 **Eocene (50-55 Ma) greenhouse climate recorded in nonmarine rocks of San Diego, CA,**
18 **USA**

19
20 Adrian P. Broz^{1,2§*}, Devin Pritchard-Peterson³, Diogo Spinola⁴, Sarah Schneider², Greg
21 Retallack², and Lucas C.R. Silva^{5,6}

22
23 ¹ Department of Earth, Atmospheric and Planetary Sciences, Purdue University, Lafayette, IN

24 ²Department of Earth Sciences, University of Oregon, Eugene, OR

25 ³Dudek Environmental Consulting, Encinitas, CA

26 ⁴Department of Chemistry and Biochemistry, University of Alaska, Fairbanks, AK

27 ⁵Environmental Studies Program, University of Oregon, Eugene, OR

28 ⁶Department of Biology, University of Oregon, Eugene, OR

29

30 ***Correspondence:** abroz@uoregon.edu

31

32 **Abstract**

33

34 Nonmarine rocks in sea cliffs of southern California store a detailed record of weathering
35 under tropical conditions millions of years ago, where today the climate is much drier and
36 cooler. This work examines early Eocene (~50-55 million-year-old) deeply weathered
37 paleosols (ancient, buried soils) exposed in marine terraces of northern San Diego County,
38 California, and uses their geochemistry and mineralogy to reconstruct climate and
39 weathering intensity during early Eocene greenhouse climates. These Eocene warm spikes
40 have been modeled as prequels for ongoing anthropogenic global warming due to a spike in
41 atmospheric CO₂. Paleocene-Eocene thermal maximum (PETM, ~55 Ma) kaolinitic paleosols
42 developed in volcanoclastic conglomerates are evidence of intense weathering (CIA >98)
43 under warm and wet conditions (mean annual temperature [MAT] of ~17° C ± 4.4° C and
44 mean annual precipitation [MAP] of ~1920 ± 182 mm). Geologically younger Early Eocene
45 climatic optimum (EECO, 50 Ma) high shrink-swell (Vertisol) paleosols developed in coarse
46 sandstones are also intensely weathered (CIA >80) with MAT estimates of ~20° C ± 4.4° C but
47 have lower estimated MAP (~1500 ± 108 mm), suggesting a less humid climate for the EECO
48 greenhouse spike than for the earlier PETM greenhouse spike.

49

50

51 **1. Introduction**

52 Periods of accentuated greenhouse conditions, characterized by spikes (or excursions) in
53 CO₂ concentrations exceeding ~2000 ppm, punctuated the Earth's climate during the
54 Paleogene, from the late Paleocene to the Early Eocene (60 to 52 million years ago) (Pearson

55 and Palmer, 2000). During these epochs, global temperatures often reached more than ten
56 degrees Celsius higher than those of the pre-industrial period (Anagnostou et al., 2016). These
57 Eocene CO₂-driven warm spikes have been modeled as prequels for ongoing anthropogenic
58 global warming (Bowen et al., 2006; Carmichael et al., 2017).

59 Paleosols (fossil soils) from the Late Paleocene to Eocene epochs have been reported
60 worldwide in Antarctica (Spinola et al., 2017), Argentina (Andrews et al., 2017), Australia (Zhou
61 et al., 2015), and across the United States (Wilf, 2000; White and Schiebout, 2008, Kelson et al.,
62 2018); These paleosols demonstrate markedly more intense weathering conditions than in
63 the same area today and are evidence of the warmer climates that prevailed during the early
64 Cenozoic (Andrews et al., 2017). Evidence of increased weathering intensity across latitudes is
65 from the formation of deep (~30 meter) weathering profiles (Abbott, 1981), elevated
66 alteration indices (Babechuck et al., 2014) and abundant kaolinite (White and Schiebout,
67 2008), which are characteristics of deeply weathered modern soils at present-day equatorial
68 to subequatorial latitudes (Butt et al., 2000). The increased weathering intensity on land
69 surfaces during these periods is a direct function of climate and is also influenced by other
70 processes such as vegetation and microbial activity (Silva and Lambers, 2021).

71 New evidence of these warming periods can be seen in a sequence of Eocene paleosols
72 located in today's coastal deserts of southern California, revealing a significantly warmer and
73 wetter paleoclimate relative to the modern arid climate. Early Eocene paleosols in the coastal
74 plains of northwestern Baja California and southwestern California show the effects of intense
75 weathering under a subtropical humid climate (Abbott, 1981). This is consistent with the
76 global greenhouse climates during the Paleocene-Eocene Thermal Maximum (PETM, ~55 Ma)
77 (Kraus et al., 2013; Bowen et al., 2014). An additional global warming event, known as the
78 Early Eocene Climatic Optimum (EECO, 52-50 Ma), also fostered intense weathering in warm,
79 wet climates (Zachos et al., 2008; Song et al., 2018).

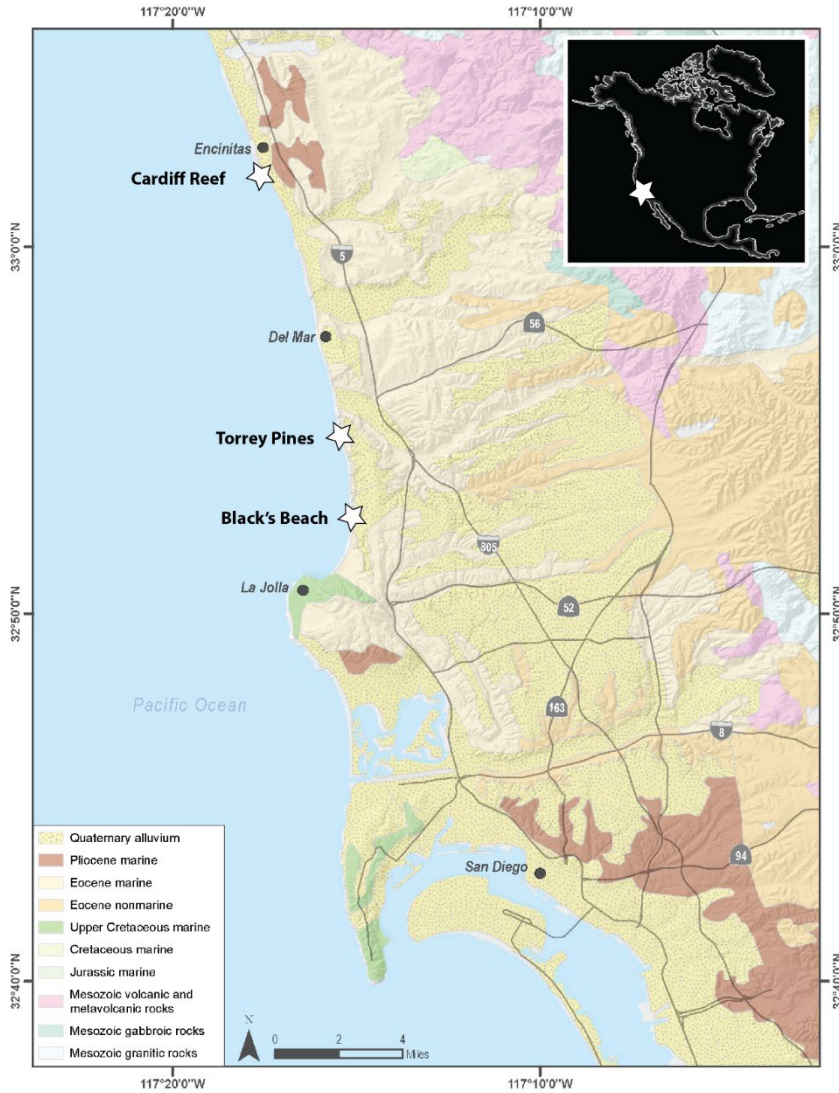
80 Although Cenozoic paleosols of San Diego have been known for several decades (Abbott,
81 1981), they are now able to be thoroughly examined using a comprehensive set of
82 climofunctions and other quantitative proxies for soil formation conditions (Sheldon et al.,
83 2002; Sheldon and Tabor, 2009; Nordt and Driese, 2010, Adams et al., 2011). Application of
84 these techniques to a new set of deeply weathered Eocene paleosols advances our
85 understanding of how Eocene climate excursions affected land surfaces across latitudes. This
86 work uses the morphology, mineralogy and geochemistry of San Diego paleosols to provide a
87 quantitative assessment of climate and weathering intensity on land during and after Eocene
88 greenhouse spikes.

89

90 **2. Geological setting and Cenozoic greenhouse climate**

91 The study area lies within the peninsular Ranges of southern California and is
92 composed primarily of Jurassic to Cretaceous igneous and metamorphic rocks (Abbott and
93 May, 1991). Erosion following mountain-building in the mid-Cretaceous led to the formation

94 of a stable, flat-lying coastal-plain basement that ranges in age from late Cretaceous to early
95 Holocene. This work focuses on two of the coastal plain stratigraphic units of upper
96 Cretaceous and early Eocene age that have preserved evidence of intense subaerial
97 alteration.



98
99 **Figure 1. Field areas in northern San Diego County, California, USA**

100
101 Shortly after the late Jurassic to mid-Cretaceous Nevadan orogeny, San Diego County
102 was transformed into a low-lying coastal plain that accumulated Cretaceous to Cenozoic
103 nonmarine and marine sedimentary deposits (Fredericksen, 1991; Abbott and May 1991).
104 Paleosols of the greater San Diego area developed on Jurassic andesite and andesitic breccia,
105 Rancho Delicias Granodiorite, as well as early Eocene [55 Ma] volcanic and volcanoclastic
106 conglomerates of the Mt. Soledad Formation. The discontinuous sequence of weathered
107 intervals begins with Paleocene (55 Ma) kaolinitic Oxisol paleosols at Rancho Delicias, Tijuana,
108 which are nearly 30 meters in vertical thickness (Abbott, 1981). Approximately 60 km to the

109 north, outcrops of early Eocene (55 Ma) kaolinitic paleosols of the Mt. Soledad conglomerate
110 are exposed in beach cliffs at Black's Beach, La Jolla, below Ardath Shale with mollusks of the
111 *Turritella uvasana* zone (Peterson and Abbott, 1979). These are overlain by Middle Eocene (50
112 Ma) smectite-rich paleosols of the marginal marine Delmar formation at San Elijo Beach,
113 Cardiff, CA. Paleosols of the Delmar Formation are overlain by late Eocene (~40 Ma) Aridisol
114 paleosols of the Friars formation that contain abundant pedogenic carbonate nodules and a
115 variety of vertebrate fossils of the Uintan North American Land mammal Age (Abbott, 1981;
116 Walsh et al. 1996). This study focused on paleosols of the early Eocene (55 Ma) Mt. Soledad
117 formation and later early Eocene (50 Ma) Delmar formation. Paleomagnetic evidence locates
118 southern California at latitudes 35-40 ° N during the Paleocene and Early Eocene (Smith and
119 Briden, 1977), at least 400 km north of its current latitude of 32° N.

120

121 **Mount Soledad Formation Conglomerate**

122 Conglomerates of the basal Mount Soledad formation are overlain by the early Middle
123 Eocene Ardath Shale (Peterson and Abbott, 1979). The Mt. Soledad formation is a framework-
124 supported, amalgamated conglomerate with exotic clast composition (Kennedy and Moore,
125 1971). The composition of the clasts is dominated by quartz phenocryst-bearing rhyolites that
126 originated from present-day Sonoran desert of Mexico as well as quartzite and silicified tuff
127 (Abbott et al., 1989). Conglomerate clasts include approximately 40% rhyolite, 26% black
128 dacites, 13% Santiago Peak Volcanics, 12% schist, 4% plutonic, and 2% intraformal (Abbott
129 and May, 1991). Paleohydrological reconstruction of the area suggested a 300-km long river
130 with a channel width of 20-80 m and a peak 100-year flood discharge of 30,000 m³ S⁻¹ (Abbott,
131 1981).

132

133 **Delmar Formation Sandstone**

134 The Eocene (50 Ma) Delmar formation consists of coarse-grained quartzofeldspathic
135 sandstone that was deposited in shallow marine, intertidal and supratidal facies of the Eocene
136 San Diego Embayment (Abbott and May, 1981), and is approximately equivalent in age to the
137 Green River Formation in Wyoming (Smith et al., 2008). Tidally influenced sedimentary
138 features include an assemblage of largely shallow marine oysters, flaser bedding, inclined
139 cross bedding, interlaminated siltstone and mudstone that follow basal and lateral
140 accretionary surfaces of tidal channels, and occasional flood and return-surge deposits
141 (Abbott and May, 1981; Eisenberg and Abbott, 1981) Fossil plants such as giant leather fern
142 (*Acrostichum aureum*) also suggest mangrove habitats (Myers, 1991).

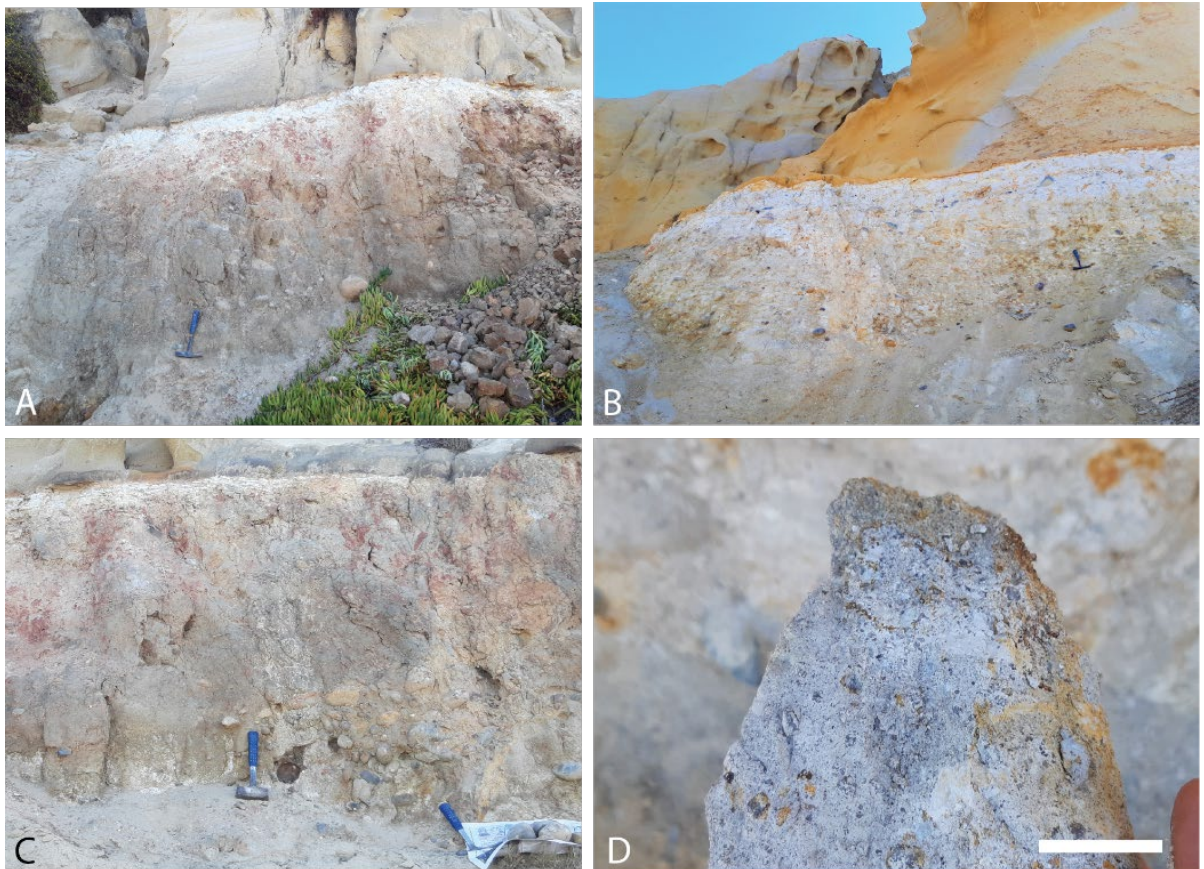
143

144 **3. Materials and Methods**

145

146 **Sample Collection and morphological assessment**

147 Field descriptions and collection of hand samples was performed at Black's Beach, La Jolla,
148 CA, USA (32.895500, -117.253520) and at San Elijo Beach, Cardiff-by-the-Sea, CA (32.895500, -
149 117.25352) (Figures 2 and 3). Five paleosol profiles were sampled. These included a
150 paleocatena of two profiles (along strike) at La Jolla, and a vertical sequence of three
151 successive profiles in Cardiff. Additional profiles of putative mangrove paleosols in supratidal
152 facies of the Delmar formation were observed at Torrey Pines, CA and descriptions are
153 included in Supplementary information. The grey paleosols with carbonaceous root traces
154 and oysters at Torrey Pines were not chemically analyzed, because unlike thick red paleosols,
155 they are not developed enough to reveal paleoclimate or other soil forming factors (Adams et
156 al., 2011). Hand samples were collected by trenching to approximately 30 cm into the
157 paleosol outcrop for fresh samples. Large, lithified blocks were collected at approximately 20
158 cm intervals, similar to sampling the horizons of a modern soil profile. The morphology,
159 qualitative grain size, Munsell color and calcareousness of samples were described during
160 collection. Paleosol taxonomic assessment followed the methods and nomenclature of U.S.
161 Soil Taxonomy (Soil Survey Staff, 2014). Pedotypes followed the nomenclature of the local
162 Kumeyaay language spoken by the 12 federally-recognized tribes of the region (Field, 2012).
163

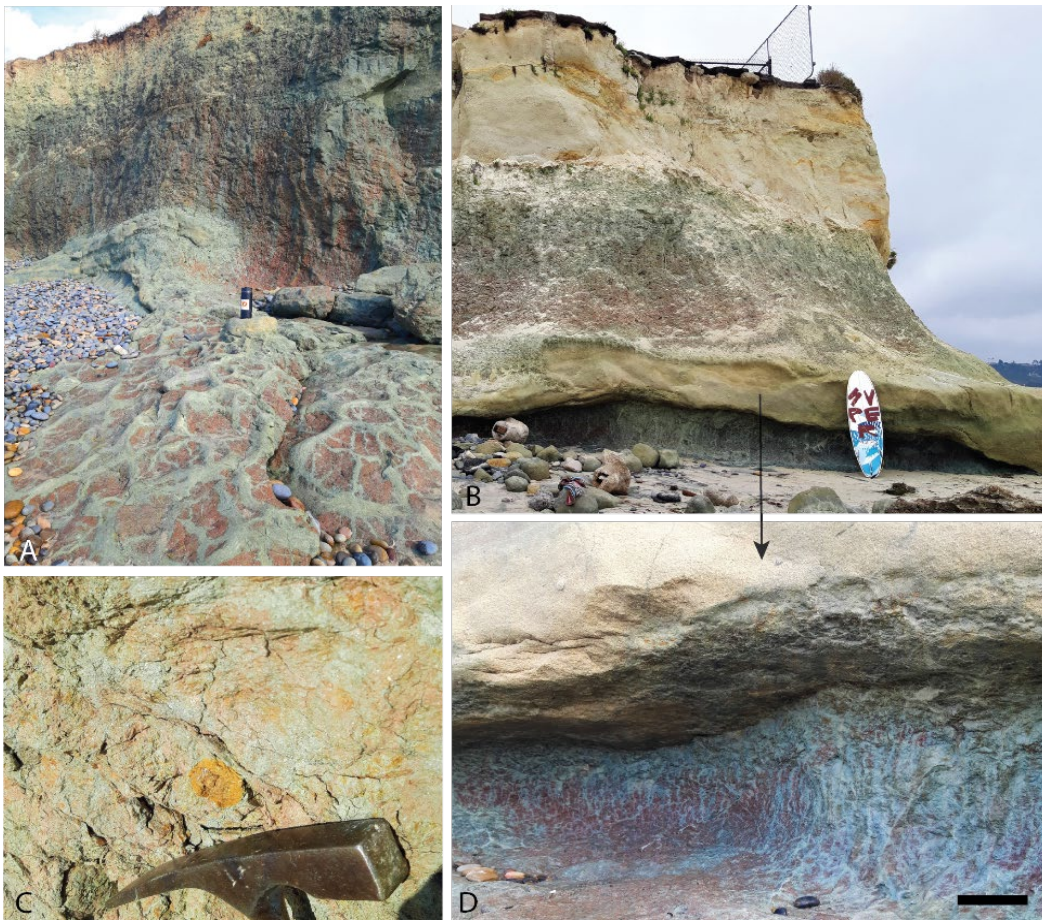


164
165
166

Figure 2. A paleocatena of two severely weathered early Eocene (55 Ma) kaolinitic paleosols in marine terrace at Black's Beach, La Jolla, California USA

167 (32.895500, -117.253520). A) White/brown kaolinitic paleosol profile formed in
168 conglomerate of the Eocene (55 Ma) Mt. Soledad formation and buried by overlying
169 Torrey formation sandstone (32.89400, -117.253520:); B) Gray/white kaolinitic profile
170 (along strike) also formed in conglomerates of the Eocene (55 Ma) Mt. Soledad
171 formation and buried by overlying Torrey formation sandstone; C) large >10 cm
172 conglomerate clasts in the C-horizon of the brown/white profile; D) hand sample from
173 the A-horizon of gray/white profile showing kaolinite (white) and residual coarse
174 quartz clasts. Scale bar in D) is 2 cm

175
176
177



178 **Figure 3. A sequence of Eocene (50 Ma) red clay Vertisol (shrink-swell) paleosols**
179 **at San Elijo Beach, Cardiff-by-the-sea, California, USA (32.895500, -117.25352).** A)
180 Three successive Vertisol paleosols exposed in marine terraces with soil structures
181 exposed in the shore platform including coarse sand-filled mudcracks; C) common Fe
182 oxide concretions up to 5 cm in diameter in the B-horizons of the lowermost two
183 profiles; D) Drab green/gray coarse sand-filled mudcracks and brick-red matrix of the
184

185 basal paleosol profile with extensive mottling extending to sea in the shore platform.
186 Scale bar in C) is 10 cm

187

188 **Bulk geochemistry**

189 Major element chemistry of paleosols was determined by X-ray fluorescence (XRF) and
190 Pratt titration for FeO at ALS Laboratories, Vancouver, British Columbia (Table S1). Errors for
191 XRF detection of individual elements (Table S1) were calculated from ten replicate
192 measurements of the standard CANMET SDMS2 (British Columbia granodioritic sand). These
193 data were used to calculate molar weathering ratios, indices of alteration, and geochemical
194 mass balance (tau, strain) of each paleosol profile. Bulk density was measured on lithified
195 clasts using the paraffin-clod method of Blake and Hartge (1986). These values are provided in
196 Tables S1 and S2.

197

198 **Geochemical Proxies**

199 The degree of weathering of paleosols can be estimated using molecular ratios as
200 indicators of the soil-forming processes (Retallack, 2019) including salinization ($\text{Na}_2\text{O}/\text{K}_2\text{O}$),
201 calcification ($\text{CaO} + \text{MgO}/\text{Al}_2\text{O}_3$), clayeyness ($\text{Al}_2\text{O}_3/\text{SiO}_2$), base loss ($\text{Al}_2\text{O}_3/$
202 $\text{CaO}+\text{MgO}+\text{Na}_2\text{O}+\text{K}_2\text{O}$) and gleization ($\text{FeO}/\text{Fe}_2\text{O}_3$). Salinization is a measure of the salt
203 accumulation in paleosols whereas calcification estimates the accumulation of pedogenic
204 carbonates at depth. Clayeyness and base loss evaluate the extent of hydrolytic weathering
205 and leaching of cations as a function of depth in the profile. Gleization constrains the redox
206 state of the soil before burial, with values > 1 suggesting waterlogged and reducing
207 conditions and values < 1 suggesting well-drained, oxidizing conditions before burial
208 (Retallack, 2019; Broz, 2020). Oxide weight percentages were also used to estimate mean
209 annual precipitation using the CIA-K (chemical index of alteration minus K_2O)
210 paleoprecipitation proxy (Sheldon et al., 2002), defined as $221.12e^{0.0197(\text{CIA-K})}$ with R^2 0.72 and
211 standard error (s.e.) of 182 mm, and the CALMAG weathering index, designed for use with
212 Vertisol paleosols (Norse and Driese, 2010), defined as $\text{Al}_2\text{O}_3/(\text{Al}_2\text{O}_3 + \text{CaO} + \text{MgO}) \times 100$. The
213 CALMAG paleoprecipitation proxy ($y=22.69x - 435.8$, $R^2 = 0.90$; s.e. ± 108 mm, where $x =$
214 CALMAG weathering index) was compared with CIA-K paleoprecipitation estimates (Sheldon
215 et al., 2002). Calculated values are provided in Table S3.

216

217

218 **Total Inorganic / Organic carbon and pH**

219 The pH and total organic carbon (TOC) of samples was assessed to constrain the organic
220 content and diagenetic history of paleosols. Since waterlogged soils can be sites of enhanced
221 organic preservation, especially those with $\text{FeO}/\text{Fe}_2\text{O}_3 < 1$ (Broz et al, 2022), we used
222 elemental analysis to quantify the paleosol organic carbon pool. However, paleosols often
223 contain both ancient and modern carbon as inferred from radiocarbon dating, and

224 distinguishing between the two can be challenging (Broz et al., 2022). Furthermore,
225 reconstructing soil pH from paleosols is difficult because diagenesis (e.g., groundwater
226 alteration) can obscure or overprint original soil pH (Lukens et al., 2018). Paleosol samples
227 were manually encapsulated in 5 × 8 mm tin capsules (sample size approximately (25–70 mg)
228 prior to elemental analysis. Total organic carbon was determined by elemental analysis on a
229 Costech ECS 4010 instrument at the University of Oregon’s Soil-Plant-Atmosphere Laboratory,
230 with expected standard deviation < 0.3%. Paleosol pH was determined by electrode in a 1:2
231 mixture of ground paleosol sample to deionized water. No pre-acidification of paleosols were
232 performed here (e.g., Harris et al., 2001), so it is possible that paleosols with pH >6.5 contained
233 some amount of inorganic carbon (e.g., carbonate). All samples were analyzed in duplicate.
234 TOC and pH values are provided in Table S4.

235

236 **Visible/near infrared spectroscopy**

237 Visible-near infrared (VNIR) spectroscopy was used to determine the alteration mineralogy of
238 select samples. Lithified hand samples of paleosols (approximately 200 g) were selected for
239 analysis. An ASD FieldSpec Pro3 reflectance spectrometer in the Planetary Surfaces
240 Laboratory at Purdue University was used to examine the reflectance spectra of samples from
241 0.35-2.50 μm. Samples were not ground or sieved before analysis. Spectra from laboratory
242 standards of kaolinite, hematite, goethite, montmorillonite and illite from the Western
243 Washington University Vis-NIR Spectroscopy Database were compared with spectra from
244 hand samples to constrain the mineralogy of unknown samples. Raw spectra are provided in
245 Table S6.

246

247 **Micromorphology**

248 Petrographic thin sections of paleosol samples were used to classify paleosol
249 micromorphology, estimate grain size distribution and constrain mineral composition
250 (Murphy, 1983). Thin sections of oriented paleosol samples were point counted using a Swift
251 automated stage and Hacker counting box fitted to a Leitz Orthoplan Pol research
252 microscope. Determination of average grain size and qualitative mineralogy with error of 2%
253 for common components (Murphy (1983). A total of 1000 points on each thin section were
254 counted (500 points for relative proportion of minerals and 500 points for determination of
255 sand, silt and clay size fractions) (**Table S7**). Thin section descriptions followed methodology
256 outlined by Stoops (2003). Focus was given to pedogenic features indicative of soil forming
257 processes (e.g., clay coatings and nodules) as well as to b-fabrics.

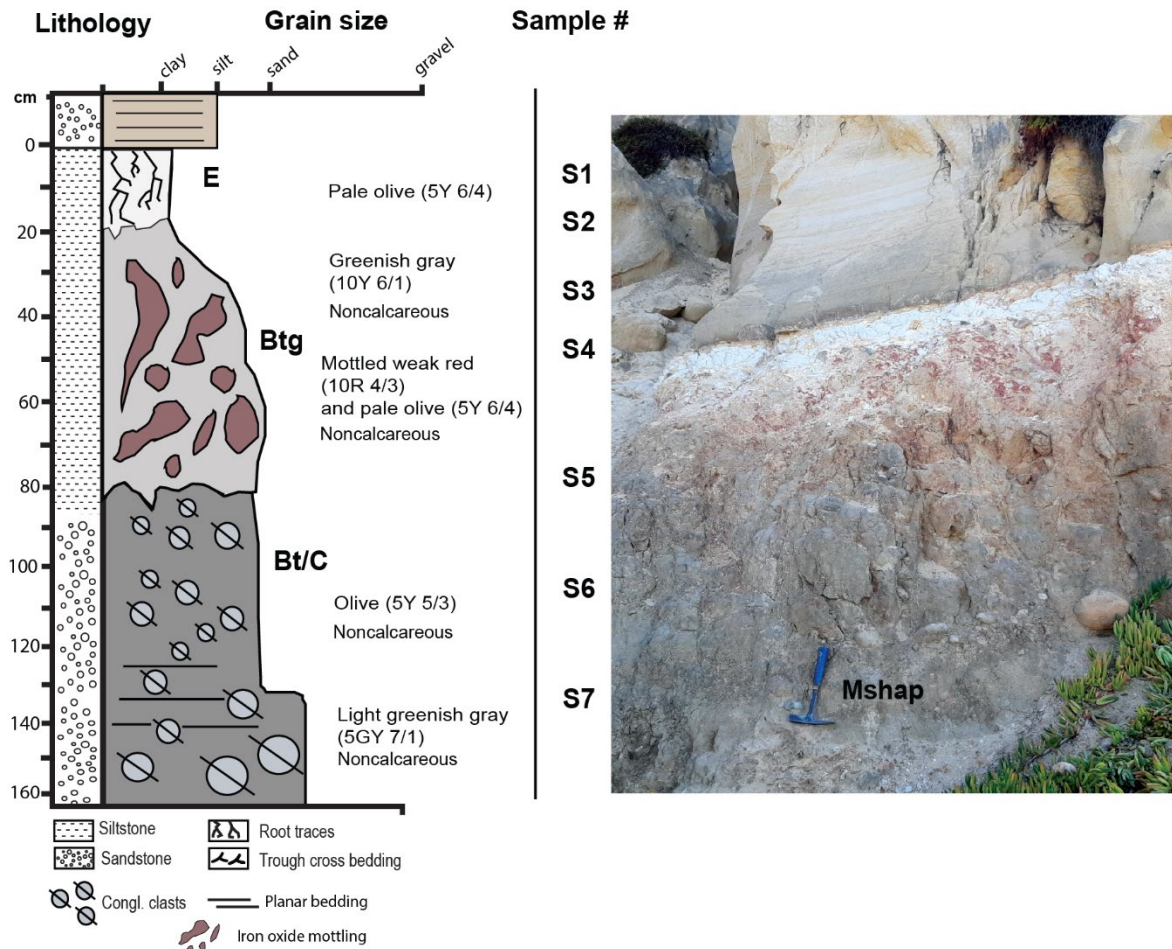
258 **4. Results and Discussion**

259 **4.1 Morphology and micromorphology**

260

261 ***Mshap (White) profile***

262 The kaolinite-rich profile analyzed in this study, herein referred to as *Mshap* ("White" in the
 263 Kumeyaay language; Field, 2012), exhibits characteristics consistent with a poorly-drained
 264 Ultisol paleosol, known as an Aquult soil in US Soil Taxonomy System (Soil Survey Staff, 2014).
 265 This profile has a kaolinitic E-horizon that gradually transitions into a well-developed, mottled
 266 B horizon distinguished by large (10 cm length) drab-haloed root traces. The bleached E
 267 horizon subtly grades into the mottled red hues of the B horizon (Figure 4), a transition
 268 suggesting intermittent saturation potentially caused by seasonal flooding. The deepest
 269 horizon (C) hosts a parent material of well-rounded chert and quartzite clasts, imbricated to
 270 the west, with diameters reaching up to 15 cm. The A-horizon of the original profile was likely
 271 removed by erosion during the deposition of the overlying sandstone. It appears that
 272 weathered conglomerate clasts extend deeper into the C-horizon of the profile (possibly 3-4
 273 meters), but views of such material were obscured by colluvium at the time profiles were
 274 observed (e.g., unweathered R-horizon of conglomerate at bottom of profile was covered by
 275 overburden and not visible), so it is possible that profiles are indeed ~3-4 meters or more in
 276 vertical thickness as noted by Abbott (1981).
 277



279 **Figure Mshap Ultisol paleosol (Aquult) at Black's Beach, La Jolla, CA**, with a kaolinitic A-
280 horizon and a mottled Btg horizon with large drab-haloed root traces. The C horizon has
281 rounded chert and quartzite clasts up to 15 cm in diameter that are imbricated to the west. All
282 clasts are well rounded.

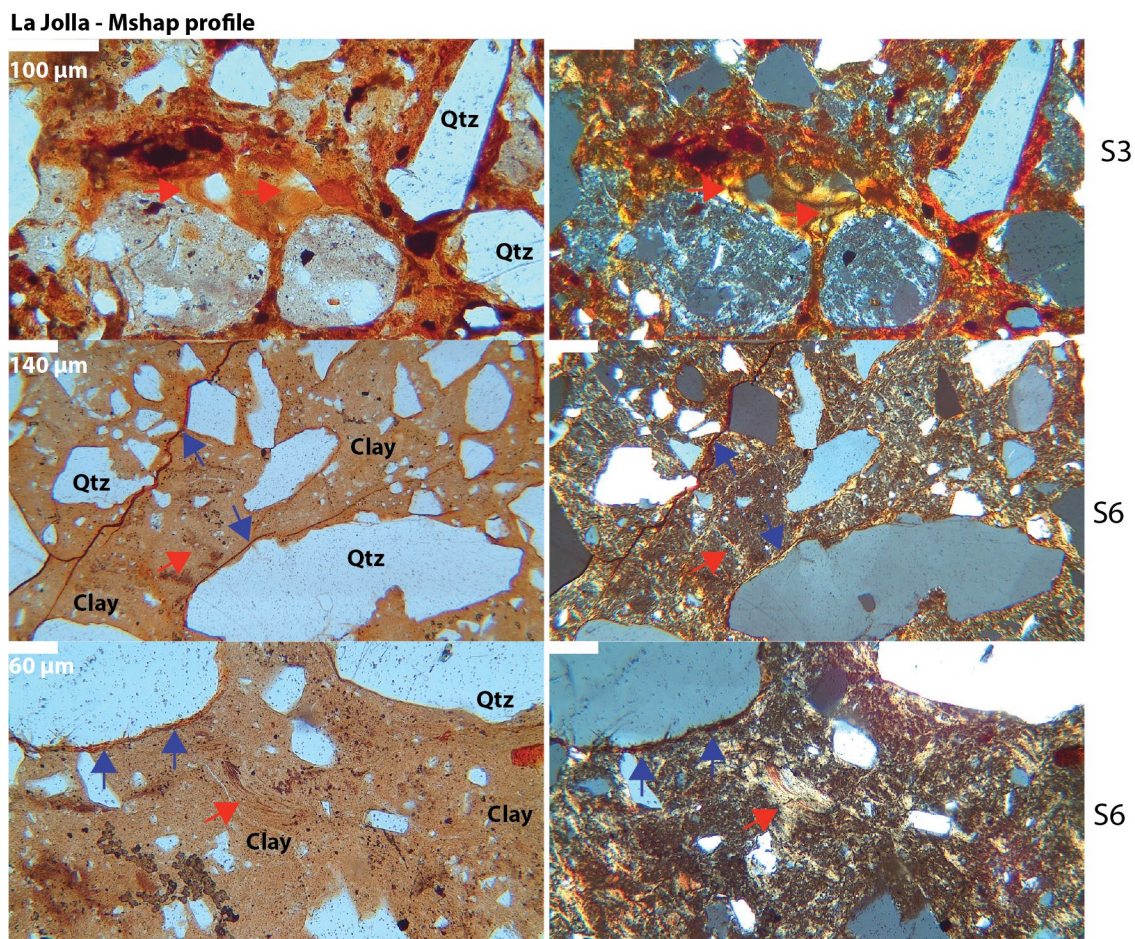
283

284 Micromorphological observations also support the hypothesis of an Aquult-like
285 paleosol (Table S8). The surface horizon visible in the outcrop has been identified as an E
286 horizon, characterized by clay and Fe depletion. A few clay coating remnants were observed
287 in several planar voids (Figure 5), while the subsurface horizons exhibited an abundance of
288 clay coatings and redoximorphic features (Figure 5).

289 The subsurface horizons have been classified as a sequence of poorly-drained argillic
290 (Btg) horizons, primarily due to the frequent presence of clay coatings, Fe nodules, and
291 depletion/impregnation features (Figure 5). The clay coatings were limpid, displaying low
292 interference colors. These coatings were frequently found associated with planar voids and
293 showed clear extinction lines, although signs of occasional disturbance such as fragmentation
294 and poor orientation were evident. We hypothesize that pedoturbation—via the
295 incorporation of clay coatings into a clayey groundmass—and post-burial deformation may
296 have been contributing factors to the disturbance of clay coatings. The presence of striated b-
297 fabrics (e.g., grano, cross, and circular) in the B horizons supports the suggestion of
298 substantial pedoturbation processes (Figure 5) (Kühn et al., 2018).

299 There was no evidence of lithological discontinuity, suggesting a continuous profile.
300 The uniformity of the parent material across all samples is indicated by the similar c/f
301 distribution, mineral composition, roundness, and sorting (Table S8). Quartz, which
302 dominates the coarse fraction, displays a predominantly wavy extinction, hinting at a
303 metamorphic origin. The intense weathering present was confirmed by the detection of
304 fractured quartz grains infilled with kaolinite and/or Fe oxides (e.g., "runiquartz", Driese et al.,
305 2018) (Table S8).

306



307

308

309 **Figure 5. Micromorphological features of the early Eocene (55 Ma) La Jolla**

310 **(Mshap) profile seen in plane polarized light (PPL, left column) and cross polarized light**

311 **(XPL, right column). Top row is E horizon showing limpid and oriented clay coatings (red**

312 **arrows) and Fe nodules (dark spots in PPL/XPL); middle row is Btg horizon showing circular**

313 **striated b-fabric (red arrow) and granostriated b-fabrics with limpid and oriented clay**

314 **coatings (blue arrows); bottom row is Btg horizon showing clay coatings (red arrow) and Fe**

315 **hypocoatings (blue arrows). Sample nomenclature in right column can be traced across all**

316 **analyses performed on samples (see Tables S1-S9)**

317

318

319 ***Hwatt* (red) profile**

320 This profile at La Jolla resembled a poorly-drained Ultisol paleosol (Aquept). Because

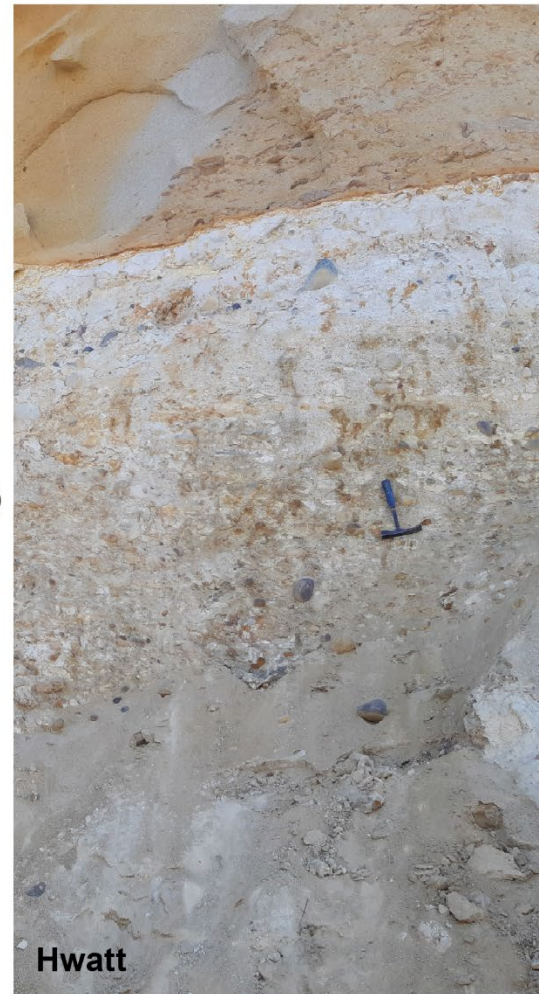
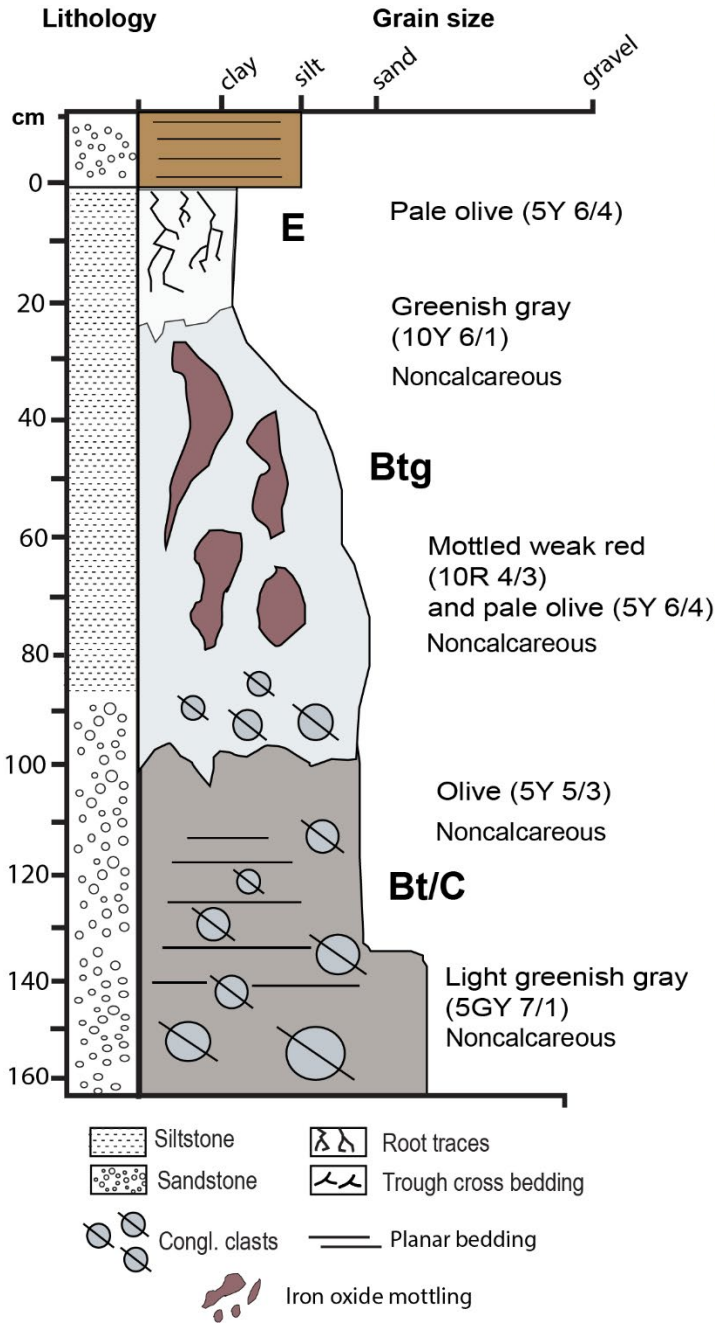
321 of the common and large red mottles, it is herein *referred to as Hwatt* ("Red" in the Kumeyaay

322 language). The bleached-white kaolinitic A-horizon contained root traces up to 2 cm in

323 diameter and reaching 18 cm in depth. This profile also has a kaolinitic A-horizon overlying a

324 mottled Bw horizon with rounded quartzite clasts up to 15 cm in diameter and a mixture of

325 sand and clay. The gray to white subsurface (B) horizon was consistent with poorly drained
 326 conditions indicated by the bleached surface grading into a mottled red subsurface indicative
 327 of seasonal waterlogging (Retallack et al., 2001). The C horizon contains well- rounded chert
 328 and quartzite clasts also imbricated to the west and up to 20 cm in diameter. The pair of
 329 paleosols described at Black’s Beach represent a paleocatena, two soils varying laterally
 330 (along strike) from the same ancient land surface, representing differences in
 331 paleotopography (e.g., hillslope vs. toeslope) (Retallack, 2019).
 332



334 **Figure 6. Poorly drained *Hwatt* paleosol (Aquult) at Black's Beach, La Jolla, CA**
335 with root traces up to 2 cm in diameter and reaching to 18 cm in depth. This profile
336 also has a kaolinitic A-horizon overlying a mottled Bw horizon with rounded quartzite
337 clasts up to 15 cm in diameter.

338

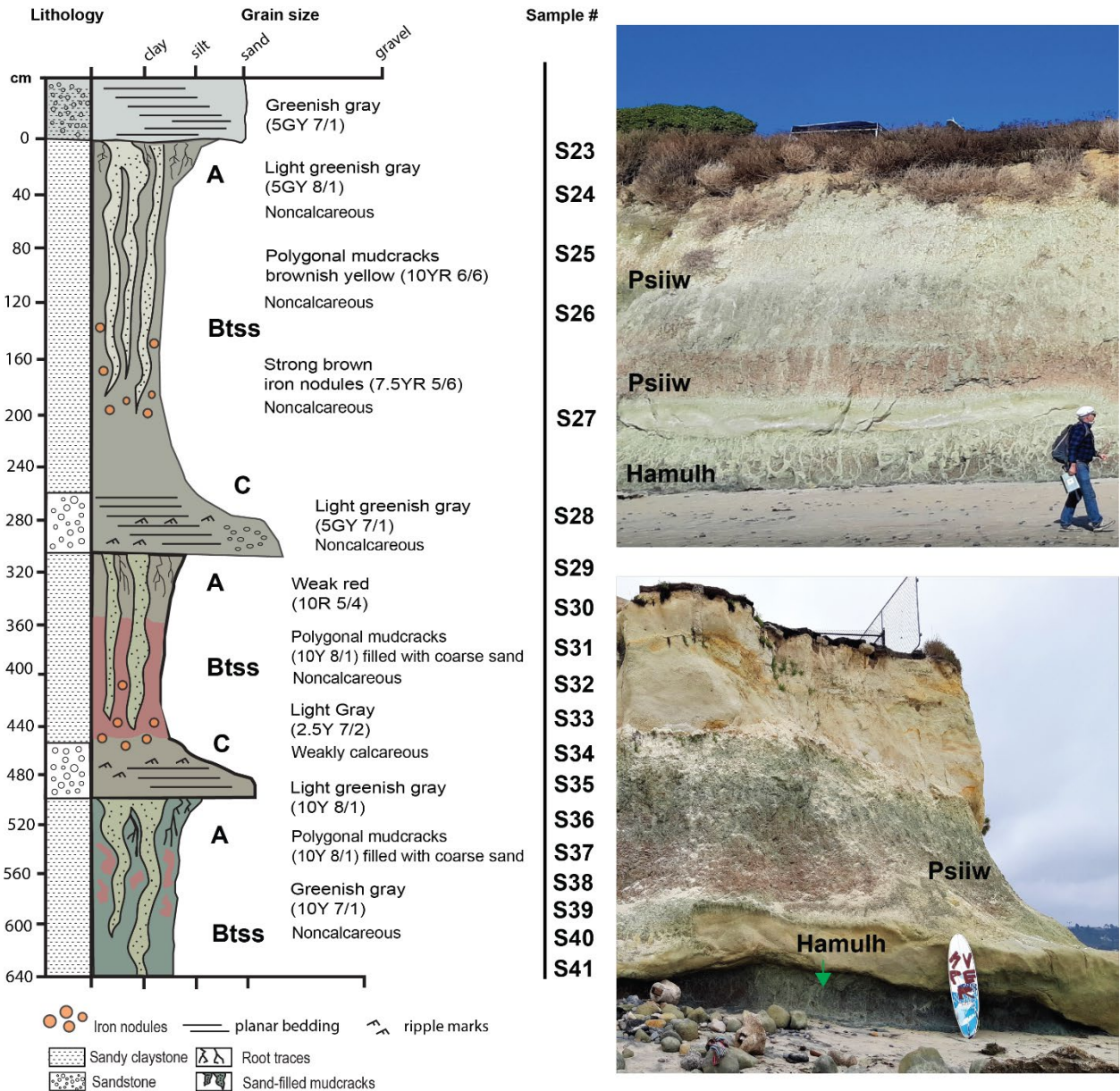
339 ***Psiiw*(Green) and *Hamulh* (Surf) profiles**

340

341 This sequence of three clay-rich paleosols at Cardiff resembled a modern Vertisol (smectitic
342 high shrink-swell soils, Soil Survey Staff, 2014), which formed on a parent material of
343 quartzofeldspathic sand. The uppermost two profiles, herein referred to as *Psiiw* or "green" in
344 Kumeyaay language (Field, 2012) overlie the basal *Hamulh* ("*Surf*") *pedotype* that composes
345 the shore platform and extends seaward. The weak red (10R 5/4) surface horizons contain
346 common and massive, sand-filled polygonal desiccation features, common slickensides
347 oriented at random angles, and abundant drab halo root traces to 4 cm in diameter and up to
348 25 cm in depth. These graded into a weak red (10R 5/4) subsurface clay horizons (Bss or Bssg
349 horizons) also with abundant slickensides, occasional clasts of coarse quartz sand, and
350 occasional Fe concretions up to 3 cm in diameter (Figure 7). The ledge-forming BC-horizon of
351 the middle profile was a light greenish gray (10Y 7/1) noncalcareous coarse-grained
352 quartzofeldspathic sandstone. This overlaid the basal profile, which was brick red (10 R 5/4)
353 and also pierced with mottled green (10Y 8/1) sand-filled cracks and root traces to 5 cm in
354 diameter with abundant slickensides. Large (75 cm depth and up to 10 cm in diameter),
355 polygonal, sand-filled mudcracks are common in other Vertisol paleosols (Driese and
356 Foreman, 1992; Driese and Ober, 2005).

357 The basal *Hamulh* paleosol profile in the shore platform extends seaward (Figure 3) and
358 creates "*Cardiff Reef*", a world-famous surfing area known for long, tapering and consistent
359 wave formation, due in part to incision of the shore platform by the San Elijo river (**Figure S1**)
360 that has created a deep offshore channel located approximately 50 m south of the Cardiff
361 study area (Ludka et al., 2019).

362



363

364

Figure 7. Sequence of red clay Vertisol (shrink-swell) paleosols in beach cliffs and shore

365

platform at San Elijo Beach, Cardiff, CA. Deep (<75 cm) coarse-sand-filled polygonal

366

mudcracks are green/gray in color (10Y 8/1) and are present in weak red (10R 5/4) soil matrix

367

with abundant slickensides and Fe-bearing concretions.

368

369

Micromorphological observations validated interpretation of these paleosols as Vertisols (Figure 8). Diagnostic vertic soil properties, including a large and well-developed blocky structure along with strongly striated b-fabrics, were consistently observed throughout the Bss horizons (Figure 8) (Kovda and Mermut, 2018).

373

The A horizons were characterized by a smaller blocky structure with a secondary granular structure, accompanied by a well-developed pore network resembling fine roots,

374

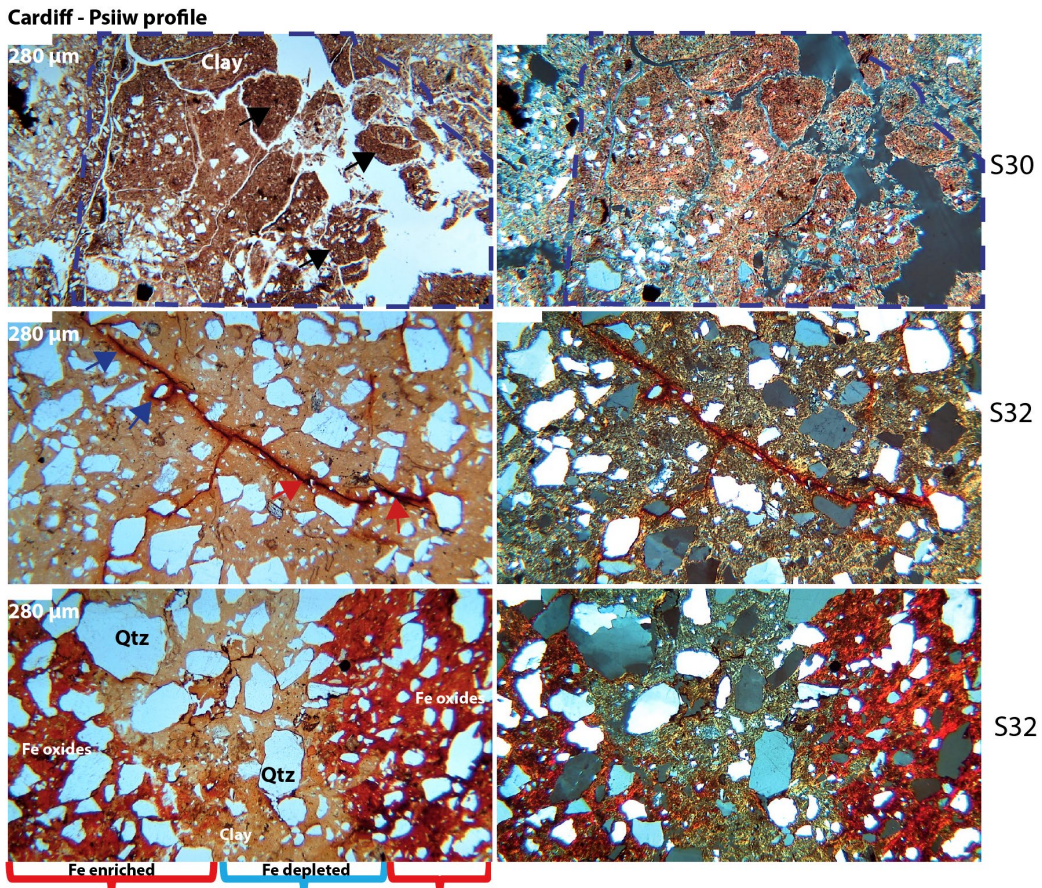
375 which likely belonged to a grassland-type vegetation. The infilling of finer textured particles
376 in larger pores suggested proximity to the surface Figure 8, top row).

377

378 We identified lithological discontinuities and buried horizons, as denoted by the
379 numerical prefix in the horizon designations and the "b" suffix, respectively. The lithological
380 discontinuities were readily discernible due to abrupt alterations in the size, sorting, and
381 composition of the coarse fraction. The buried horizons were identified by the sudden
382 reappearance of A horizon properties, such as an extensively developed pore system
383 resembling roots and material infilling.

384 Overall, this paleosol sequence demonstrated relatively good drainage, and only a few
385 horizons showed redoximorphic features like Fe coatings, nodules, and an Fe-depleted
386 groundmass (Fig. X). Unlike the La Jolla profiles, the Cardiff profiles demonstrated a more
387 diverse mineral composition, predominantly featuring quartz with a frequent occurrence of
388 biotite and plagioclase. Notably, no instances of runiquartz formation were detected (Table
389 S8).

390



391

392 **Figure 8. Micromorphological features of the Eocene (50 Ma) Cardiff (Psiw)**
393 **profile seen in plane polarized light (PPL, left column) and cross polarized light (XPL,**

394 **right column).** Top row shows A-horizon with subangular blocky ped structure (black arrows)
395 and clay mineral accumulation; note well developed-pore network with finer material
396 indicated by dashed blue line; middle row shows Btss horizon with well-developed b-fabric
397 (yellow in PPL) and Fe-oxide lined pore network; red arrows indicate inner Fe matrix and blue
398 arrows indicate outer diffuse Fe matrix boundary; bottom row shows Btss horizon with
399 residual quartz and Fe enriched areas (red brackets) alternating with Fe depleted areas (blue
400 bracket). Sample nomenclature in right column can be traced across all analyses performed
401 on samples (Tables S1-S9)

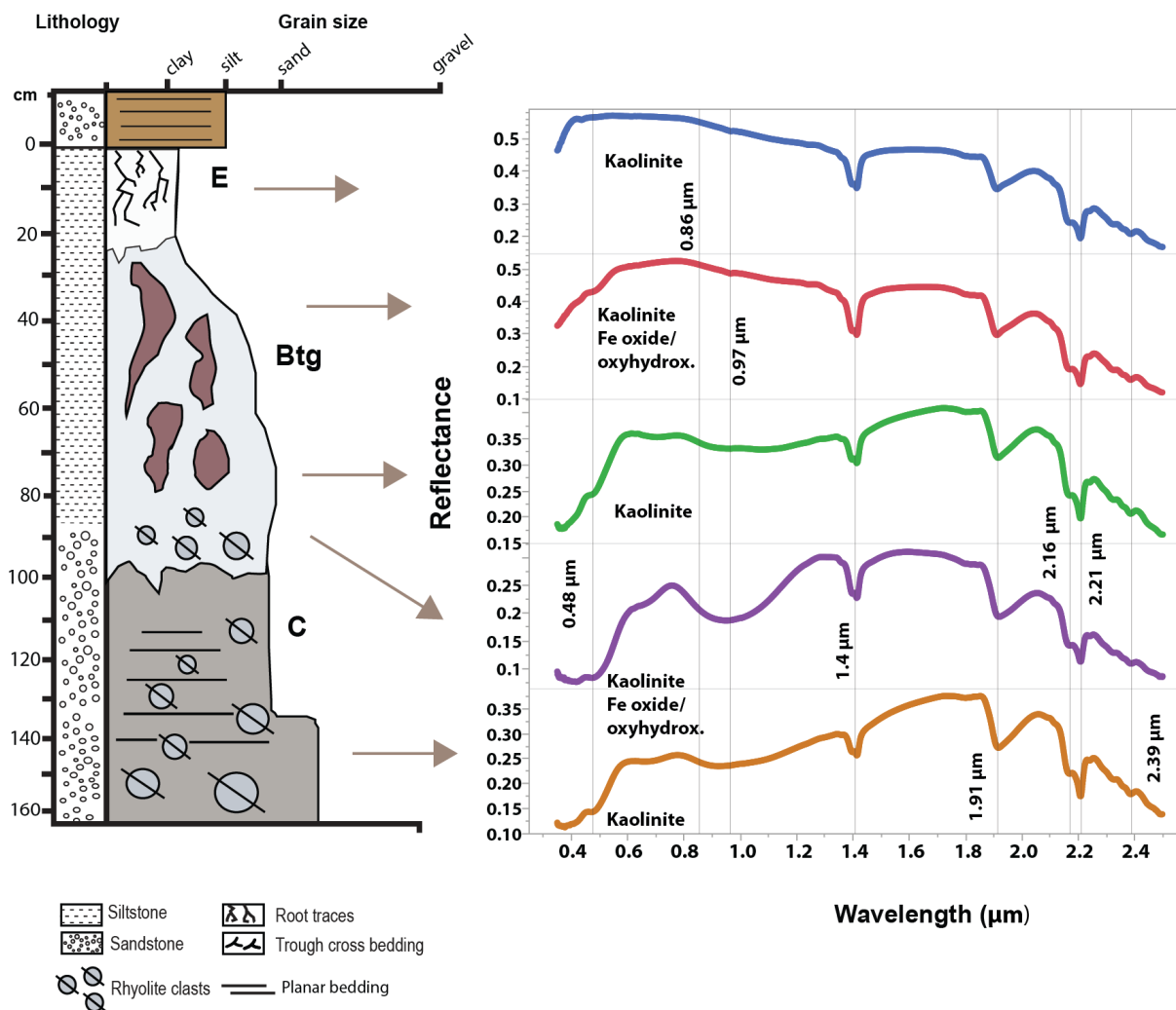
402
403

404 **Visible/near infrared spectroscopy**

405 Analysis of the Mshap paleosol (La Jolla) showed strong absorptions with band centers
406 near 0.5, 0.8 1.41, 1.9, 2.16, 2.2, and 2.39 μm (Figure 9). We interpret these absorptions as
407 kaolin-group minerals (kaolinite, halloysite, dickite) with contributions from Fe oxides and a
408 Fe^{3+} -bearing phyllosilicate. The absorptions at 1.41 μm are indicative of the first kaolinite
409 overtone whereas the 1.9 μm band is from a combination tone of Al-OH bending and H-O-H
410 stretching in H_2O (Goudge et al., 2015) or from the presence of another hydrated phase. A
411 shoulder exists at 2.16 as a doublet with the 2.20 μm band, which is caused by a combination
412 tone of the OH stretch (Bishop et al., 2008) and is diagnostic of kaolinite (e.g., Ye and
413 Michalski, 2022). A band near 2.39 μm could also be consistent with OH stretching and
414 bending combinations in a Fe^{3+} phyllosilicate, possibly due to the isomorphic substitution of
415 Al or Fe for Si in the tetrahedral layers, or from cation bonding between tetrahedral and
416 octahedral layers (Bishop et al., 2008).

417 The presence of finely crystalline Fe oxides in the lower Mshap profile was inferred
418 from absorption features centered near 0.5 μm and a broad feature near 0.85 μm (Haber et al.,
419 2022). The C horizon had the most pronounced Fe oxide features with the largest band depth
420 at 0.85 μm noted across all samples. Fe oxides features were mainly observed in the
421 subsurface horizons and were absent in the surface (E horizon) samples. This suggests that
422 the surface horizon may have been poorly drained and chemically reducing whereas the
423 subsurface may have been well-drained and more oxidized.

424



425

426 **Figure 9. Visible-near infrared spectroscopy of the La Jolla Ultisol paleosol.**

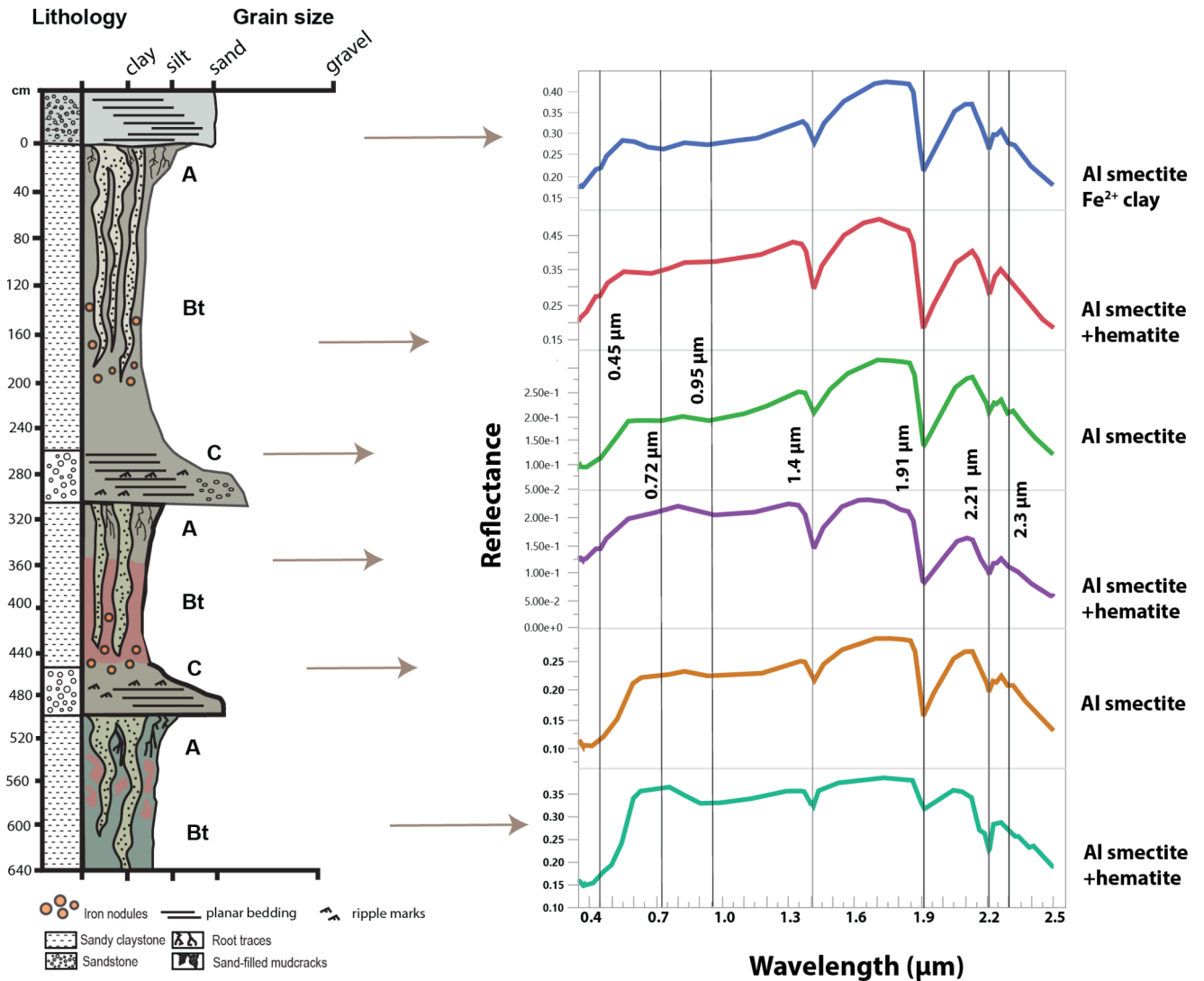
427 Absorption features highlighted at 0.48, 0.86, 0.97, 1.4, 1.95 μm , as well as the doublet feature
 428 at 2.16 and 2.2 μm , are consistent with kaolinite and Fe oxides and/or oxyhydroxides

429

430 The Hamulh and Psiiw paleosols (Cardiff) had absorptions with band centers at 1.4,
 431 1.91, 2.21 and $\sim 2.35 \mu\text{m}$. The absorption features at 1.91 and 2.21 μm were consistent with a
 432 strongly crystalline Al smectite (e.g., Al montmorillonite). The absorptions at 1.4 μm and 1.9
 433 μm were similar to kaolinite, but the kaolinite-diagnostic doublet feature at 2.16 and 2.2 μm
 434 was absent in all but one of the Cardiff samples. Instead, an absorption feature near $\sim 2.35 \mu\text{m}$
 435 was consistent with Fe^{2+} -rich phyllosilicates such as zinnwaldite and/or chamosite, or a mixed
 436 layer illite-smectite (Bishop et al., 2008).

437 Despite the extensive green-red mottling in the Cardiff paleosols, Fe oxide signatures
 438 were largely absent in visible wavelengths. Only one sample, the A-horizon of the lowermost
 439 profile, had absorption features centered near 0.5 and 0.8 μm , characteristic of Fe oxides such
 440 as hematite. Interestingly, the lowermost profile was the reddest of the three profiles and

441 suggested it may have been less affected by early diagenetic burial gleization (Retallack,
 442 1991). This process may have converted a significant portion of the Fe oxides and
 443 oxyhydroxides from the ferric state to a drab-colored ferrous state, and since ferrous iron is
 444 much more soluble, may have resulted in depletion of total iron in the profiles (Retallack,
 445 1991). This may be why we did not see strong Fe oxide signatures in most samples despite
 446 the inferred presence of ferric iron characteristic of deeply weathered soils (Brown et al.,
 447 2006).



448 **Figure 10. Visible-near infrared spectroscopy of three Vertisol paleosol profiles (red**
 449 **Hamulh and green Psiiw pedotypes) from Cardiff-by-the-sea, CA. Absorption features**
 450 **highlighted at 0.45, 0.74, 1.4, 1.91, 2.21 and 2.3 μm are consistent with Al smectite and**
 451 **hematite**
 452

453
 454 Paleosols at both localities showed chemical weathering trends consistent with
 455 extensive leaching and subaerial alteration (Figure 11). The *Hwatt* Ultisol-like paleosol (La

456 Jolla) showed only slight salinization ($\text{Na}_2\text{O}/\text{K}_2\text{O}$) and calcification ($\text{CaO}+\text{MgO}/\text{Al}_2\text{O}_3$) with
457 values less than 0.15 (Figure 11A). On the other hand, we observed moderate clayeyness
458 ($\text{Al}_2\text{O}_3/\text{SiO}_2$) in the uppermost horizon with values up to 0.4 that decreased to 0.2 in the
459 subsurface (Bt and C) horizons. Base loss followed a similar trend where the highest values
460 (~ 40) were noted in the near-surface horizons and decreased to values less than 20 in the C
461 horizon. Gleization, indicative of waterlogging before burial, was greatest in the surface (E)
462 horizon and decreased with depth. Low salinization and calcification values (~ 0.1) were noted
463 and are common in Ultisols of wet climates where precipitation exceeds evapotranspiration
464 (Retallack, 2019). Clayeyness and base loss were highest in the near-surface horizons of the
465 paleosol, indicative of subaerial alteration and leaching, but overall values were less than
466 would be expected for a more deeply weathered Oxisol. Gleization values of ~ 0.5 in the A-
467 horizon also suggest waterlogging conditions before burial and are consistent with seasonal
468 saturation by surface water. A decrease of $\text{FeO}/\text{Fe}_2\text{O}_3$ in the subsurface horizons suggests
469 perched surface water rather than groundwater was responsible for the seasonal
470 waterlogging conditions.

471

472 **Chemical Weathering Trends**

473 The Cardiff Vertisol paleosols (*Psiiw and Hamulh*) had salinization and calcification
474 values up to ~ 4 and 0.2, respectively, with the highest values in the A horizons of both profiles
475 (Figure 11B). Moderate salinization suggests that precipitation was not adequate to remove
476 most Na_2O , especially when compared to the low salinization values of the La Jolla (*Hwatt*)
477 profile. Low calcification values (up to 0.2) were similar to the Hwatt profile, suggesting an
478 absence of pedogenic carbonate. Vertisols of wet climates such as those examined here (MAP
479 $> \sim 1000$ mm) do not typically contain pedogenic carbonate whereas Vertisols of dry climates
480 (MAP < 1000 mm) can accumulate pedogenic carbonate in subsurface (i.e., Bssk) horizons
481 (Driese et al., 2000), leading to increased calcification values (Retallack, 2019). On the other
482 hand, base loss in the Cardiff Vertisols was an order of magnitude lower than the Hwatt
483 paleosol (base loss values of 1-4 versus 40). These base loss values are consistent with other
484 observations of Cambrian Vertisol paleosols from South Australia (Retallack, 2009) and
485 suggest lower weathering intensity compared to the *Hwatt* profile. Lastly, gleization was
486 highest in the paleosurface horizons of both profiles, suggesting either seasonal saturation
487 during pedogenesis or burial-induced diagenesis such as burial gleization (PiPujol and
488 Buurman, 1994). Burial gleization is envisaged as the reduction of Fe by anaerobic microbes
489 shortly after burial (Broz et al., 2022). In both cases, accumulation of FeO is limited to the near-
490 surface horizons (e.g., the paleosurface).

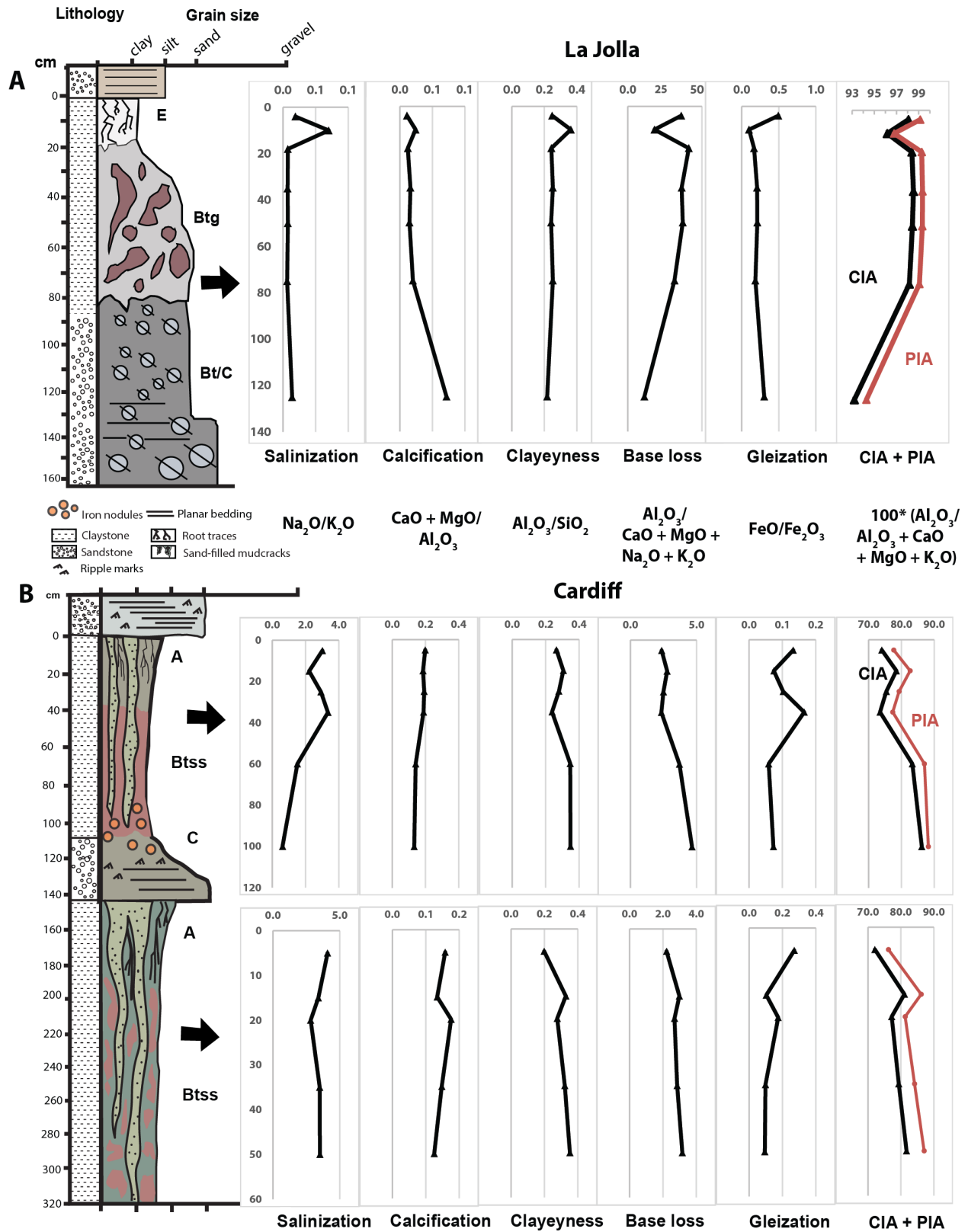
491

492 **Chemical Index of Alteration**

493 The geochemistry of the Mshap paleosol (La Jolla) showed extensive depletion of mobile
494 cations (Ca, Mg, K, Na) and a chemical index of alteration minus potassium (CIA-K) of > 98 in

495 the near-surface horizon (Figure 11A). The profile was nearly devoid of all mobile cations and
496 was significantly enriched in Si and Al. The paleosurface horizons (A and Bt) had the highest
497 CIA-K observed in the study with average values of ~99 that decreased to ~93 in the
498 subsurface (Bt/C) horizon. These high CIA values are indicative of nearly complete
499 kaolinitization, typical of highly weathered soils and paleosols (Nesbitt and Young, 1982;
500 Babechuk et al., 2014).

501 The Hamulh and Psiiw Cardiff paleosols sequence (50 Ma) was less intensely
502 weathered relative to the Eocene La Jolla paleosol (55 Ma), though with significant depletion
503 of Ca, Mg, K, and Na, and CIA-K values ranging from ~77-88 (Figure 11B). The CIA was greatest
504 in the lower A and upper Bss horizons of both profiles. Though not as intensely weathered
505 relative to the La Jolla paleosol, the accumulation of Fe oxides and massive vertic features
506 including sand-filled cracks also indicate extensive leaching under a warm, humid and
507 seasonally dry climate. The less intense weathering of Cardiff paleosols were supported by
508 micromorphological observations where biotite and plagioclase were detected, while only
509 quartz was detected in the La Jolla paleosols.



510

511

512

Figure 11. Geochemical trends of paleosols from La Jolla and Cardiff-by-the-Sea, CA. A) Geochemical trends with depth in a kaolinitic Ultisol from Black's Beach, La Jolla, CA; and **B)**

513 Vertisol (high shrink-swell) paleosols from San Elijo Beach, Cardiff by-the-sea, CA. CIA,
514 Chemical index of alteration ($100 \times [\text{Al}_2\text{O}_3 / (\text{Al}_2\text{O}_3 + \text{MgO} + \text{CaO} + \text{K}_2\text{O})]$); PIA, Plagioclase index of
515 alteration ($100 \times [\text{Al}_2\text{O}_3 - \text{K}_2\text{O} / (\text{Al}_2\text{O}_3 + \text{MgO} + \text{CaO} - \text{K}_2\text{O})]$)

516
517 La Jolla Ultisol paleosols had total organic carbon (TOC) ranging from 0.026 - 0.079 (\pm
518 0.003) wt. % and pH ranging from 3.523 - 6.283 (\pm 0.018), indicating highly acidic tropical
519 weathering conditions (**Table S2**). Like modern soil profiles, the organic carbon content was
520 enriched in the surface horizons of paleosols (E horizon) and subsequently depleted in the
521 lower horizon (C horizon). It should be noted that paleosol pH is often compromised by late-
522 stage groundwater alteration, which can reset the original pH (Lukens et al., 2018), so caution
523 is needed for primary interpretation of paleo-pH reconstruction from direct measurements of
524 pH. However, modern Oxisols and Ultisols are characterized by low pH as a result of intense
525 weathering and the generation of organic acids (Lawrence et al., 2013; Driese et al., 2018), so
526 perhaps the pH values we measured represent minimal post-diagenetic groundwater
527 alteration and thus reflect the paleo-pH of the La Jolla Profile. Alternatively, there could have
528 been late diagenetic groundwater alteration with acidic fluids, but we find this hypothesis
529 less likely due to the dearth of evidence representing early diagenetic intense weathering
530 conditions.

531 Diagenetic additions of recent/modern organic C can inflate the so-called “preserved” organic
532 C (Broz et al., 2023), but enrichments of TOC in uppermost horizons of paleosols are
533 consistent with preservation of endogenous organic C (Broz et al., 2022). Thus, it is possible
534 that organic C and paleo-pH were preserved in the La Jolla profile, though additions of small
535 amounts of geologically recent/ modern carbon are possible and perhaps likely.

536 Cardiff Hamulh and Psiw Vertisol paleosols had TOC ranging from 0.019 - 0.074 (\pm
537 0.003) wt. % and pH ranging from 7.373 - 8.907 (\pm 0.023) (Table S2). Like modern soil profiles,
538 the organic carbon content was enriched in the surface horizons of paleosols (A and Bt) and
539 subsequently depleted in the lower horizons (C horizon). The Cardiff pH results (pH > 8 in
540 some Btss/C-horizons, Table S4) suggest possible late-stage groundwater alteration (e.g.,
541 saltwater brines in shore platform) to increase alkalinity in these profiles, as it is unlikely that
542 Vertisols had such alkaline pH during soil formation unless they formed in relatively dry
543 climates (MAP < ~1000 mm) which would allow for the formation pedogenic carbonate (Broz
544 et al., 2021). Since there was no pedogenic carbonate observed in any of the Cardiff profiles, it
545 is likely that the elevated pH is due to late diagenesis (Lukens et al., 2018). The diagenetic
546 history of these paleosols is outlined in the following section.

547

548 **Diagenetic Alteration**

549 Burial diagenesis is commonly observed in paleosols and particularly affects pre-
550 Quaternary paleosols. The main diagenetic processes can range from minor (burial
551 decomposition of organic matter) to severe (contact metamorphism) (Retallack, 2001). Four

552 types of diagenetic alteration that have affected paleosols in this work are burial reddening,
553 illitization of smectite, burial gleization, and burial decomposition of organic matter.

554 The diagenetic process of burial reddening refers to the dehydration of Fe
555 oxyhydroxides (e.g., goethite, ferrihydrite) and subsequent formation of Fe oxides such as
556 hematite (Spinola et al., 2018). This most likely affected the Cardiff Vertisol profiles (**Figure 3**).
557 Modern smectite-rich Vertisols are commonly dark brown to orange in color due to
558 accumulation of goethite and Mn-bearing phases (Driese et al., 2000; Soil Survey Staff, 2014)
559 rather than the brick-red Cardiff paleosol profiles. Alternatively, the Fe oxide minerals may
560 not have formed from burial diagenesis and instead formed during pedogenic alteration
561 before burial, but such accumulation of Fe oxide and subsequent red color is more
562 characteristic of well-drained, highly weathered, non shrink-swell soils (Ultisols, Oxisols) rather
563 than Al/Fe smectite-bearing Vertisols (Chen et al., 2018; Driese et al., 2018).

564 Illitization of smectite (potash metasomatism) is common in paleosols that are subject
565 to burial diagenesis (Novoselov et al., 2015; Fedo et al., 1995) and involves the incorporation
566 of K into the crystalline structure of smectite clays such as montmorillonite and nontronite (Li
567 et al., 2016; Broz et al., 2022). Evidence for illitization of smectite in the La Jolla kaolinitic
568 profiles included VNIR absorbance features at ~2.35 microns (Figure 8), which is consistent
569 with mixtures of kaolinite and illite (Bishop et al., 2008; Ehlmann et al., 2011) or a mixed layer
570 illite-smectite clay. Alternatively, illite can be derived from the weathering of muscovite and
571 not formed from metasomatic processes (Ehlmann et al., 2011), so caution is necessary in
572 interpreting the origin of illite in these profiles. In any case, further analytical work (e.g.,
573 quantitative x-ray diffraction) is needed to support the hypothesis of diagenetic illite in
574 profiles examined in this work.

575 The striking green-red mottling observed in the paleosurface horizons of the Cardiff
576 paleosols likely resulted from alteration after burial. Burial gleization, a form of early
577 diagenesis, is thought to result from microbial reduction of Fe oxides under hypoxic or anoxic
578 conditions shortly after burial (PiPujol and Buurman, 1994; Retallack, 2019). It most commonly
579 manifests as green-gray color mottling and is restricted to the paleosurface horizons where
580 organic matter is concentrated (e.g., A-horizons). It can be distinguished from groundwater
581 alteration or other primary redoximorphic features by its confinement to the A-horizon of
582 paleosols (PiPujol and Buurman, 1994), whereas groundwater alteration from a fluctuating
583 water table introduces gley colors to the lower parts of the profile (B and C horizons)
584 (Retallack, 1991, 2019).

585 Burial decomposition of organic matter affects most all paleosols, but is more
586 pronounced in those forming under oxidizing, well-drained conditions before burial
587 (Retallack, 2019; Broz, 2020). This phenomenon, which is thought to be a form of early
588 diagenesis, can lead to severe losses of organic carbon in profiles that were once rich in
589 organic matter. We observed evidence of burial decomposition of carbon because the TOC in
590 all samples (< 0.1 wt.%) was two to three orders of magnitude lower than would be expected

591 in comparable modern Ultisols and Vertisols of subtropical climates (Broz, 2020). Redox state
592 before burial, inferred from the ratio of FeO/ Fe₂O₃, is related to the TOC content of paleosols
593 (Broz, 2020) and can provide a first-order control on the preservation of organic carbon in
594 ancient soils. Generally paleosols forming under reducing conditions (FeO/ Fe₂O₃ > 0.5) have
595 significantly higher TOC relative to more oxidized profiles with FeO/ Fe₂O₃ < 0.5 (Broz, 2020).
596 Indeed, samples with higher FeO/Fe₂O₃ such as the surface (A) horizon of the La Jolla paleosol
597 (*Hwatt*, Figure 11) had significantly more organic carbon (~0.07 wt. TOC %) (**Table S4**) relative
598 to samples with lower FeO/ Fe₂O₃, (~0.03 wt. %) providing additional evidence that redox
599 state before burial is related to organic preservation in paleosols.

600 A summary of the soil forming factors is provided in Table 1. Kaolinite-bearing *Hwatt*
601 and *Mshap* profiles at La Jolla were similar to Aquults US Soil taxonomy, with bleached
602 surfaced horizons and weakly developed (Bw) subsurface clay horizons characteristic of a
603 seasonally wet coastal lowland landscapes. Similar soils with CIA >95 and bleached surface
604 horizons form under warm, humid and everwet conditions characteristic of single-tier tropical
605 forests. Poorly drained *Hwatt* paleosols could have formed beneath a seasonally dry swamp
606 forest in a wet coastal lowland whereas the *Mshap* profiles on well-drained alluvial terraces
607 supporting a single tier tropical forest. *Psiiw* and *Hamulh* Vertisol paleosols at Cardiff likely
608 formed under warm, humid and seasonally dry conditions on a parent material of
609 quartzofeldspathic silt/ sand and possibly supported a tropical seasonally dry woodland.

610

611 Table 1. Summary of La Jolla and Cardiff paleosol interpretations

Pedotype	Location	Soil Taxonomy	FAO Map	Australia	Climate	Organisms	Topography	Parent Material
"Hwatt" "Red"	La Jolla	Aquult	Dystric Gleyisol	Humic Gley	Not diagnostic	Seasonally dry swamp forest	Seasonally wet coastal lowland	Conglomerate
"Mshap" "White"	La Jolla	Aquult	Dystric Cambisol	Brown Earth	Humid, everwet Warm, humid, seasonally dry	Tropical forest, single tier	Well-drained alluvial terrace	Conglomerate
"Psiiw" "Green"	Cardiff	Vertisol	Vertisol	Red Clay	Warm, humid, seasonally dry	Seasonally dry tropical woodland	Well-drained coastal terrace	Quartzofelspathic silt and sand
"Hamulh" "Surf"	Cardiff	Vertisol	Vertisol	Red Clay	Warm, humid, seasonally dry	Seasonally dry tropical woodland	Well-drained coastal terrace	Quartzofelspathic silt and sand

Geochemical climofunctions and implications for early Eocene climate

Paleoclimate estimates relating CIA-K (chemical index of alteration minus potassium) to mean annual precipitation (Sheldon et al 2016) are shown in Table 2. We used CIA-K to account for the possible influence of potash metasomatism (illitization of smectite) on CIA values (Novoselov et al., 2015). Samples from the Bt horizon of the Paleocene-Eocene Thermal Maximum (PETM, 55 Ma) Mshap profile in La Jolla yielded mean annual temperature (MAT) estimates of 17.5-17.7° C ± 4.4° C and mean annual precipitation (MAP) of 1779-1808 mm ± 172 mm, consistent with a humid subtropical climate. The early Eocene Climatic Optimum (EECO, 50 Ma) Psiiw and Hamulh profiles in Cardiff yielded MAT estimates of 19.8-20.6 °C ± 4.4 °C and mean annual precipitation (MAP) of 1186-1280 mm ± 172 mm, also consistent with a subtropical humid climate. Evidence for seasonality of precipitation was inferred from vertic features including large sand-filled mudcracks, suggesting a summer-dry EECO climate.

Paleoprecipitation was estimated using the CALMAG transfer function, specifically designed for use in Vertisol paleosols (Nordt and Driese et al., 2010). The Cardiff Vertisols had higher estimated MAP values ranging from 1494-1565 ± 108 mm/yr. This is consistent with the phenomenon of underestimation of paleoprecipitation using CIA-K in Vertisols of wet climates (Nordt and Driese, 2010). Together, these estimates suggest a possibly everwet tropical PETM paleoclimate that became warmer and drier in the EECO. Paleoclimate estimates of both localities therefore provide additional evidence of multiple episodes of warm and wet tropical Eocene climates.

Table 2. Geochemical climofunctions from A and B horizons of early Eocene (55 Ma) paleosol from La Jolla, CA and Eocene (50 Ma) paleosols from Cardiff, CA. Chemical index of alteration (CIA) and plagioclase index of alteration (PIA) were used to calculate estimates of paleotemperature (error) and paleoprecipitation during soil formation using transfer functions outlined in Sheldon et al (2016) based on a database of modern soils ($R^2 = 0.72$, s.e = 182 mm). The CALMAG weathering index, designed for use with Vertisol paleosols (Norse and Driese, 2010), is defined as $Al_2O_3 / (Al_2O_3 + CaO + MgO) \times 100$ and the resulting transfer function ($R^2 = 0.9$, s.e. = 108 mm) was compared with CIA-K paleoprecipitation estimates (Sheldon et al., 2016).

Location	Age (Ma)	Depth (cm)	Horizon	CIA	CIA-K	CALMAG	Paleotemp. (°C, Sheldon et al. 2002)	Paleoprecip. (mm/yr) Sheldon et al. 2002)	CALMAG paleoprecip. (mm/yr)
La Jolla	55	10	Btg	96.2	96.8	97.6	17.7	1724.8	1779.7
La Jolla	55	18	Btg	98.4	99.3	98.8	17.5	1902.7	1805.9
Cardiff	50	25	Btss	75.4	79.3	83.9	20.9	1186.8	1467.5
Cardiff	50	35	Btss	73.5	77.3	84.1	20.8	1191.9	1473.4
Cardiff	50	60	Btss	83.3	87.0	87.6	19.9	1266.4	1552.2
Cardiff	50	15	Btss	81.1	86.2	88.2	19.8	1280.2	1565.0
Cardiff	50	20	Btss	77.2	81.3	85.1	20.6	1210.0	1494.1
Cardiff	50	35	Btss	79.3	84.2	87.1	20.0	1255.0	1541.2

The range of early Eocene rainfall and temperature estimates presented in this work are consistent with previous calculations of paleotemperature and paleoprecipitation from early Eocene fossils and paleosols (Figure 12). These include CIA-K derived estimates of temperature from PETM paleosols in Argentina ($15\text{ °C} \pm 4.4\text{ °C}$, Andrews et al., 2017) and fossil leaf-margin derived analysis from Bighorn Basin, Wyoming of $19.8 \pm 3.1\text{ °C}$. Additional estimations from fossil flora of the middle Wasatchian (~52 Ma) in Wyoming range from MAT of 21 °C and MAP of nearly 1400 mm (Wilf, 2000) are closer to the Cardiff Vertisol paleosols (Table 2). From a mineralogical perspective, the presence of potentially abundant kaolinite in La Jolla paleosols (Figure 8) is also similar to PETM paleosols from Texas (White and Schiebout, 2008), Argentina (Sol Raigemborn et al., 2022) and Australia (Zhou et al., 2015).

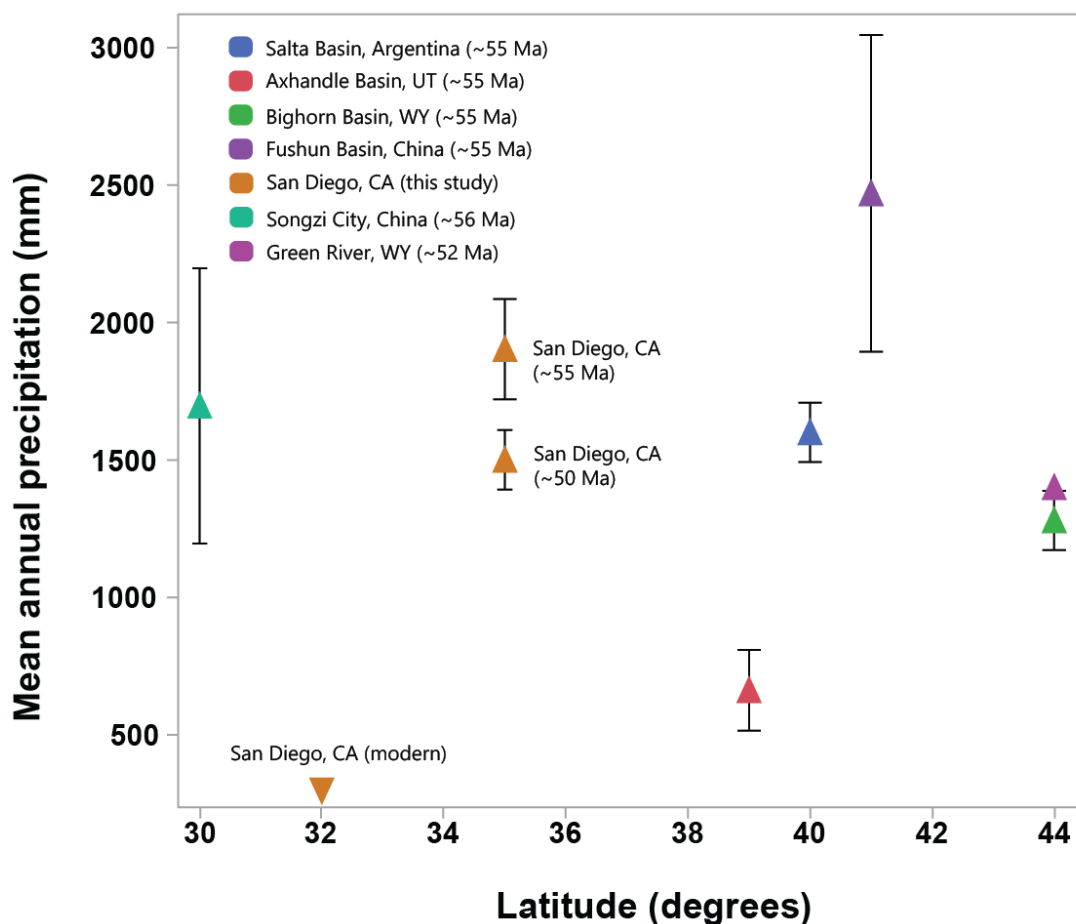


Figure 12. Comparisons of paleoprecipitation versus latitude during early Eocene greenhouse climates (~55 – 50 Ma) and comparisons with modern climate in present-day San Diego, CA. Mean annual precipitation (MAP) estimates are from Argentina paleosols (Andrews et al., 2017), Axhandle Basin, Utah paleosols (Retallack, 2005), Bighorn Basin, Wyoming paleosols (Adams et al., 2011), fossil plants of Fushun Basin, China (Chen et al., 2020); fossil pollen near Songzi City, China (Xie et al., 2022), and fossil plants of the Green River Basin, Wyoming (Wilf, 2000). Error on paleolatitude is approximately $\pm 5^\circ$. Note paleolatitude of Argentina site is $\sim 40^\circ$ S

The seasonally dry and Al smectite- rich Cardiff Vertisols are consistent with a decrease in MAP (Table 2) after the PETM and seasonality of precipitation at paleolatitudes of 35-45° N during the EECO (Hyland et al., 2018). Such seasonality of precipitation is also consistent with previous EECO observations from fluvial sediments (Wang et al., 2011; Gall et al., 2017), paleosols (Song et al., 2018) and fossils (Lowe et al., 2018). Estimations of climate from early Eocene coastal paleosols of Southern California therefore provide a new locality for paleoclimate reconstructions as well as for quantifying the nature and intensity of early Eocene weathering on land in present-day southern California.

Conclusion

Deeply weathered paleosols from the Eocene (55 Ma) Mt. Soledad Formation and the Eocene (50 Ma) Delmar formation near San Diego, CA provide new evidence of a subtropical humid climate in southern California during and after the Paleocene-Eocene thermal maximum. Early Eocene (~55 Ma) kaolinitic Ultisol paleosols developed in volcanoclastic conglomerates were subject to intense subaerial alteration and leaching with CIA-K near 99, MAT of $\sim 17^{\circ}\text{C} \pm 4.4^{\circ}\text{C}$ and MAP of $\sim 1920 \pm 182$ mm, characteristic of severe weathering under subhumid tropical conditions for thousands of years. Geologically younger Early Eocene (50 Ma) smectitic Vertisol paleosols developed atop coarse sandstones are also intensely weathered (CIA >80) and yield MAT estimates of $\sim 20^{\circ}\text{C} \pm 4.4^{\circ}\text{C}$ but with lower estimated MAP ($\sim 1500 \pm 108$ mm) and evidence for seasonality of precipitation. This may have been due to a decline in weathering intensity over ~5 Ma, or a difference in soil-forming factors other than climate such as topography or time of formation. Paleosols examined in this work represent maximum sea level regression in the Eocene of present-day southern California and also reveal a CO₂ greenhouse spike of tropical weathering conditions on land surfaces.

Acknowledgements

Pat Abbot provided invaluable guidance and knowledge in support of this project. Discussions with Briony Horgan, Clemont Royer, Roger Wiens, Jeff Johnson and Candice Bedford aided with data interpretations. Margaret Field assisted with *Kumeyaay* translation. We are also grateful for Emily Huckstead who assisted with laboratory measurements.

References

- Abbott, P.L., 1981, Cenozoic Paleosols of the San Diego Area, California: *Catena*, v. 8, p. 223–237.
- Abbott, P.L., Diego, S., and Smith, T.E., 1989, Sonora, Mexico, source for the Eocene Poway Conglomerate of southern California: *Geology*, v. 17, p. 329–332.
- Abbott, P.L., and Jeffrey A. May, 1991, Eocene Geologic History: San Diego Region: SEPM Pacific Section.
- Anagnostou, E. et al. Changing atmospheric CO₂ concentration was the primary driver of early Cenozoic climate. *Nature* 533, 380–384 (2016).
- Andrews, E., White, T., and del Papa, C., 2017, Paleosol-based paleoclimate reconstruction of the Paleocene-Eocene Thermal Maximum, northern Argentina: *Palaeogeography, Palaeoclimatology, Palaeoecology*, v. 471, p. 181–195, doi:10.1016/j.palaeo.2017.01.042.
- Bishop, J.L., Lane, M.D., Dyar, M.D., and Brown, A.J., 2008, Reflectance and emission spectroscopy study of four groups of phyllosilicates: smectites, kaolinite-serpentines, chlorites and micas: *Clay Minerals*, v. 43, p. 35–54, doi:10.1180/claymin.2008.043.1.03.

- Bowen, G.J., Maibauer, B.J., Kraus, M.J., Röhl, U., Westerhold, T., Steimke, A., Gingerich, P.D., Wing, S.L., and Clyde, W.C., 2014, Two massive, rapid releases of carbon during the onset of the Palaeocene-Eocene thermal maximum: *Nature Geoscience*, v. 8, p. 44–47, doi:10.1038/ngeo2316.
- Brimhall, G.H., and Dietrich, W.E., 1987, Constitutive mass balance relations between chemical composition, volume, density, porosity, and strain in metasomatic hydrochemical systems: Results on weathering and pedogenesis: *Geochimica et Cosmochimica Acta*, v. 51, p. 567–587, doi:10.1016/0016-7037(87)90070-6.
- Brown, D.J., Shepherd, K.D., Walsh, M.G., Mays, M.D., and Reinsch, T.G., 2006, Global soil characterization with VNIR diffuse reflectance spectroscopy: *Geoderma*, v. 132, p. 273–290, doi:10.1016/j.geoderma.2005.04.025.
- Broz, A.P., 2020, Organic Matter Preservation in Ancient Soils of Earth and Mars: *Life*, v. 10, doi:doi:10.3390/life10070113.
- Broz, A.P., Clark, J., Sutter, B., Ming, D.W., Tu, V., Horgan, B., and Silva, L.C.R., 2022, Mineralogy and diagenesis of Mars-analog paleosols from eastern Oregon, USA: *Icarus*, v. 380, p. 114965, doi:10.1016/j.icarus.2022.114965.
- Broz, A. P. *et al.* Detection of organic carbon in Mars-analog paleosols with thermal and evolved gas analysis. *J. Geophys. Res. Planets* (2022)
doi:<https://doi.org/10.1029/2022JE007340>.
- Broz, A., Aguilar, J., Xu, X. & Silva, L. C. R. Accumulation of radiocarbon in ancient landscapes: A small but significant input of unknown origin. *Sci. Rep.* **13**, 1–12 (2023).
- Butt, C. R. M., Lintern, M. J. & Anand, R. R. Evolution of regoliths and landscapes in deeply weathered terrain — implications for geochemical exploration. *Ore Geol. Rev.* **16**, 167–183 (2000).
- Chen, C., Barcellos, D., Richter, D.D., Schroeder, P.A., and Thompson, A., 2018, Redoximorphic Bt horizons of the Calhoun CZO soils exhibit depth-dependent iron-oxide crystallinity: *Journal of Soils and Sediments*,
- Chen, Z. et al. Spatial change of precipitation in response to the Paleocene-Eocene thermal Maximum warming in China. *Glob. Planet. Change* 194, 103313 (2020).
- Drese, S.G., Simpson, E.L., Eriksson, K.A., and Block, E., 1995, Redoximorphic paleosols in alluvial and lacustrine deposits, 1.8 Ga Lochness Formation, Mount Isa, Australia: Pedogenic Processes and Implications for Paleoclimate: *Journal of Sedimentary Research*, p. 675–679.
- Driese, S.G., and Foreman, J.L., 1992, Paleopedology and paleoclimatic implications of late Ordovician vertic paleosols, Juniata Formation, southern Appalachians: *Journal of Sedimentary Petrology*, v. 62, p. 71–83, doi:10.1306/D4267893-2B26-11D7-8648000102C1865D.
- Driese, S.G., Medaris, L.G., Kirsimäe, K., Somelar, P., and Stinchcomb, G.E., 2018, Oxisolic processes and geochemical constraints on duration of weathering for Neoproterozoic Baltic paleosol: *Precambrian Research*, v. 310, p. 165–178, doi:10.1016/j.precamres.2018.02.020.
- Driese, S.G., Mora, C.I., Stiles, C.A., Joeckel, R.M., and Nordt, L.C., 2000, Mass-balance reconstruction of a modern Vertisol : implications for interpreting the geochemistry and burial alteration of paleo-Vertisols: *Geoderma*, v. 95, p. 179–204.

- Driese, S.G., and Ober, E.G., 2005, Paleopedologic and paleohydrologic records of precipitation seasonality from early Pennsylvanian "Underclay" paleosols, U.S.A: *Journal of Sedimentary Research*, v. 75, p. 997–1010, doi:10.2110/jsr.2005.075.
- Ehlmann, B.L., Mustard, J.F., Clark, R.N., Swayze, G.A., and Murchie, S.L., 2011, Evidence for low-grade metamorphism, hydrothermal alteration, and diagenesis on Mars from phyllosilicate mineral assemblages: *Clays and Clay Minerals*, v. 59, p. 359–377, doi:10.1346/CCMN.2011.0590402.
- Field, M., 2012, Kumeyaay language variation, group identity, and the land: *International Journal of American Linguistics*, v. 78, p. 557–573, doi:10.1086/667451.
- Fredericksen, N., 1991, Age determinations for Eocene formations of the San Diego California area based on pollen data: *SEPM Pacific Section*, p. 195.
- Gall, R. D., Birgenheier, L. P. & Berg, M. D. Vanden. Highly Seasonal And Perennial Fluvial Facies: Implications for Climatic Control on the Douglas Creek and Parachute Creek Members, Green River Formation, Southeastern Uinta Basin, Utah ,U.S.A . *J. Sediment. Res.* **87**, 1019–1047 (2017).
- Goudge, T.A., Mustard, J.F., Head, J.W., Fassett, C.I., and Sandra, M., 2015, Assessing the Mineralogy of the Watershed and Fan Deposits of the Jezero Crater Paleolake System , Mars: *Journal of Geophysical Research – Planets*, doi:10.1002/2014JE004782.
- Haber, J.T., Horgan, B., Fraeman, A.A., Johnson, J.R., Wellington, D., Cloutis, E., and Jacob, S., 2022, Mineralogy of a Possible Ancient Lakeshore in the Sutton Island Member of Mt . Sharp , Gale Crater , Mars , From Mastcam Multispectral Images: *Journal of Geophysical Research: Planets*, v. 127, doi:10.1029/2022JE007357.
- Harris, D., Horwáth, W.R., and van Kessel, C., 2001, Acid fumigation of soils to remove carbonates prior to total organic carbon or CARBON-13 isotopic analysis: *Soil Science Society of America Journal*, v. 65, p. 1853–1856, doi:10.2136/sssaj2001.1853.
- Hyland, E. G., Huntington, K. W., Sheldon, N. D. & Reichgelt, T. Temperature seasonality in the North American continental interior during the Early Eocene Climatic Optimum. *Clim. Past* **14**, 1391–1404 (2018).
- Kelson, J. R. *et al.* Warm Terrestrial Subtropics During the Paleocene and Eocene: Carbonate Clumped Isotope ($\Delta 47$) Evidence from the Tornillo Basin, Texas (USA). *Paleoceanogr. Paleoclimatology* **33**, 1230–1249 (2018).
- Kennedy, M.P., and Moore, G.W., 1971, Stratigraphic Relations of Upper Cretaceous and Eocene Formations, Son Diego Coastal Area , California. *American Association of Petroleum Geologists Bulletin*, v. 5, p. 709–722.
- Kovda, I. & Mermut, A. R. *Vertic Features. Interpretation of Micromorphological Features of Soils and Regoliths* (Elsevier B.V., 2018). doi:10.1016/b978-0-444-63522-8.00021-8.
- Kraus, M.J., McInerney, F.A., Wing, S.L., Secord, R., Baczynski, A.A., and Bloch, J.I., 2013, Paleohydrologic response to continental warming during the Paleocene-Eocene Thermal Maximum, Bighorn Basin, Wyoming: *Palaeogeography, Palaeoclimatology, Palaeoecology*, v. 370, p. 196–208, doi:10.1016/j.palaeo.2012.12.008.
- Kraus, M. J. & Riggins, S. Transient drying during the Paleocene-Eocene Thermal Maximum (PETM): Analysis of paleosols in the bighorn basin, Wyoming. *Palaeogeogr. Palaeoclimatol. Palaeoecol.* **245**, 444–461 (2007).
- Kühn, P., Aguilar, J., Miedema, R. & Bronnikova, M. *Textural Pedofeatures and Related*

- Horizons. Interpretation of Micromorphological Features of Soils and Regoliths* (Elsevier B.V., 2018). doi:10.1016/b978-0-444-63522-8.00014-0.
- Lawrence, C., Harden, J. & Maher, K. Modeling the influence of organic acids on soil weathering. *Geochim. Cosmochim. Acta* **139**, 487–507 (2014).
- Li, Y., Cai, J., Song, M., Ji, J., and Bao, Y., 2016, Influence of organic matter on smectite illitization : A comparison between red and dark mudstones from the Dongying Depression , China: *American Mineralogist*, v. 101, p. 134–145.
- Lowe, A. J. *et al.* Plant community ecology and climate on an upland volcanic landscape during the Early Eocene Climatic Optimum : McAbee Fossil Beds , British. *Palaeogeogr. Palaeoclimatol. Palaeoecol.* **511**, 433–448 (2018).
- Ludka, B.C. et al., 2019, Sixteen years of bathymetry and waves at San Diego beaches: *Nature Scientific Data*, v. 6, p. 1–13, doi:10.1038/s41597-019-0167-6.
- Lukens, W.E., Nordt, L.C., Stinchcomb, G.E., Driese, S.G., and Tubbs, J.D., 2018, Reconstructing pH of paleosols using geochemical proxies: *Journal of Geology*, v. 126, p. 427–449, doi:10.1086/697693.
- Murphy, C.P., 1983, Point counting pores and illuvial clay in thin section: *Geoderma*, v. 31, p. 133–150, doi:10.1016/0016-7061(83)90004-6.
- Nesbitt, H. & Young, G. . Early Proterozoic climates and plate motions inferred from major elements chemistry of lutites. *Nature* **299**, 715–717 (1982).
- Nordt, L.C., and Driese, S.D., 2010, New weathering index improves paleorainfall estimates from Vertisols: *Geology*, v. 38, p. 407–410, doi:10.1130/G30689.1.
- Novoselov, A.A., Roberto, C., and Filho, D.S., 2015, Potassium metasomatism of Precambrian paleosols: *Precambrian Research*, v. 262, p. 67–83, doi:10.1016/j.precamres.2015.02.024.
- Pearson, P. N. & Palmer, M. R. Atmospheric carbon dioxide concentrations over the past 60 million years. *Nature* **406**, 695–699 (2000).
- Peterson, G., and Abbott, P., 1979, Mid-eocene climatic change, southwestern california and northwestern baja california: *Paleogeography, Paleoclimatology, Paleoecology*, v. 26, p. 73–87.
- PiPujol, M.D., and Buurman, P., 1994, The distinction between ground-water gley and surface-water gley phenomena in Tertiary paleosols of the Ebro basin, NE Spain: *Palaeogeography, Palaeoclimatology, Palaeoecology*, v. 110, p. 103–113, doi:10.1016/0031-0182(94)90112-0.
- Retallack, G.J., 2009, Cambrian paleosols and landscapes of South Australia: *Australian Journal of Earth Sciences*:, p. 37–41, doi:10.1080/08120090802266568.
- Retallack, G.J., 2019, *Soil of the Past*: Wiley Blackwell.
- Retallack, G.J., 1991, Untangling the effects of burial alteration and ancient soil formation: *Annual Review of Earth and Planetary Sciences*, p. 183–206.
- Retallack, G. J. Pedogenic carbonate proxies for amount and seasonality of precipitation in paleosols. 333–336 (2005) doi:10.1130/G21263.1.
- Retallack, G.J., Bestland, E., and Fremd, T., 2000, Eocene and Oligocene Paleosols of Central Oregon: *Geological Society of America Special Paper*, v. 344, p. 1–192, doi:10.1046/j.1365-3091.2001.0394c.x.
- Sheldon, N.D., Retallack, G.J., and Tanaka, S., 2002, Geochemical Climofunctions from North American Soils and Application to Paleosols across the Eocene - Oligocene Boundary in

- Oregon Geochemical Climofunctions from North American Soils and Application to Paleosols across the Eocene-Oligocene Boundary in Or: *The Journal of Geology*, v. 110, p. 687–696, doi:10.1086/342865.
- Silva, L. C. R. & Lambers, H. Soil-plant-atmosphere interactions: structure , function , and predictive scaling for climate change mitigation. *Plant Soil* (2020) doi:10.1007/s11104-020-04427-1.
- Smith, M.E., Carroll, A.R., and Singer, B.S., 2008, Synoptic reconstruction of a major ancient lake system : Eocene Green River Formation , western United States: *GSA Bulletin*, p. 54–84, doi:10.1130/B26073.1.
- Sol Raigemborn, M., Lizzoli, S., Hyland, E., Cotton, J., Gómez Peral, L.E., Beilinson, E., and Krause, J.M., 2022, A paleopedological approach to understanding Eocene environmental conditions in southern Patagonia, Argentina: *Palaeogeography, Palaeoclimatology, Palaeoecology*, v. 601, doi:10.1016/j.palaeo.2022.111129.
- Song, B., Zhang, K., Zhang, L., Ji, J., Hong, H., Wei, Y., Xu, Y., Algeo, T.J., and Wang, C., 2018, Qaidam Basin paleosols reflect climate and weathering intensity on the northeastern Tibetan Plateau during the Early Eocene Climatic Optimum: *Palaeogeography, Palaeoclimatology, Palaeoecology*, v. 512, p. 6–22, doi:10.1016/j.palaeo.2018.03.027.
- Spinola, D.N., Portes, R. de C., Srivastava, P., Torrent, J., Barrón, V., and Kühn, P., 2018, Diagenetic reddening of Early Eocene paleosols on King George Island, Antarctica: *Geoderma*, v. 315, p. 149–159, doi:10.1016/j.geoderma.2017.11.010.
- Staff, S.S., 2014, *Keys to Soil Taxonomy*: United States Department of Agriculture, v. 12.
- Wang, C. W., Hong, H. L., Song, B. W., Yin, K. & Li, Z. H. The early-Eocene climate optimum (EECO) event in the Qaidam basin, northwest China: clay evidence. *Clay Miner.* 46, 649–661 (2011).
- White, P.D., and Schiebout, J., 2008, Paleogene paleosols and changes in pedogenesis during the initial Eocene thermal maximum : Big Bend National Park , Texas , USA C24r: *GSA Bulletin*, p. 1347–1361, doi:10.1130/B25987.1.
- Wilf, P., 2000, Late paleocene-early eocene climate changes in Southwestern Wyoming: Paleobotanical analysis: *Bulletin of the Geological Society of America*, v. 112, p. 292–307, doi:10.1130/0016-7606(2000)112<292:LPECCI>2.0.CO;2.
- Ye, B. & Michalski, J. R. Chemical weathering over hundreds of millions of years of greenhouse conditions on Mars. *Commun. Earth Environ.* **3**, (2022).
- Xie, Y., Wu, F. & Fang, X. A transient south subtropical forest ecosystem in central China driven by rapid global warming during the Paleocene-Eocene Thermal Maximum. *Gondwana Res.* **101**, 192–202 (2022).
- Zachos, J.C., Dickens, G.R., and Zeebe, R.E., 2008, An early Cenozoic perspective on greenhouse warming and carbon-cycle dynamics: *Nature*, v. 451, p. 279–283, doi:10.1038/nature06588.
- Zhou, Y., Retallack, G.J., and Huang, C., 2015, Early Eocene paleosol developed from basalt in southeastern Australia: implications for paleoclimate: *Arabian Journal of Geosciences*, v. 8, p. 1281–1290, doi:10.1007/s12517-014-1328-8.